



**HAL**  
open science

# Cold Pools Observed during EUREC4A: Detection and Characterization from Atmospheric Soundings

Ludovic Touzé-Peiffer, Raphaela Vogel, Nicolas Rochetin

► **To cite this version:**

Ludovic Touzé-Peiffer, Raphaela Vogel, Nicolas Rochetin. Cold Pools Observed during EUREC4A: Detection and Characterization from Atmospheric Soundings. *Journal of Applied Meteorology and Climatology*, 2022, 61, pp.593-610. 10.1175/JAMC-D-21-0048.1 . insu-03726899

**HAL Id: insu-03726899**

**<https://insu.hal.science/insu-03726899>**

Submitted on 21 Feb 2024

**HAL** is a multi-disciplinary open access archive for the deposit and dissemination of scientific research documents, whether they are published or not. The documents may come from teaching and research institutions in France or abroad, or from public or private research centers.

L'archive ouverte pluridisciplinaire **HAL**, est destinée au dépôt et à la diffusion de documents scientifiques de niveau recherche, publiés ou non, émanant des établissements d'enseignement et de recherche français ou étrangers, des laboratoires publics ou privés.

# Cold Pools Observed during EUREC<sup>4</sup>A: Detection and Characterization from Atmospheric Soundings

LUDOVIC TOUZÉ-PEIFFER,<sup>a</sup> RAPHAELA VOGEL,<sup>a</sup> AND NICOLAS ROCHETIN<sup>b</sup>

<sup>a</sup> LMD/IPSL, CNRS, Sorbonne University, Paris, France

<sup>b</sup> LMD/IPSL, CNRS, ENS, Paris, France

(Manuscript received 14 December 2020, in final form 13 February 2022)

**ABSTRACT:** A new method is developed to detect cold pools from atmospheric soundings over tropical oceans and applied to sounding data from the Elucidating the Role of Cloud–Circulation Coupling in Climate (EUREC<sup>4</sup>A) field campaign, which took place south and east of Barbados in January–February 2020. The proposed method uses soundings to discriminate cold pools from their surroundings: cold pools are defined as regions where the mixed-layer height is smaller than 400 m. The method is first tested against 2D surface temperature and precipitation fields in a realistic high-resolution simulation over the western tropical Atlantic Ocean. Then, the method is applied to a dataset of 1068 atmospheric profiles from dropsondes (launched from two aircraft) and 1105 from radiosondes (launched from an array of four ships and the Barbados Cloud Observatory). We show that 7% of the EUREC<sup>4</sup>A soundings fell into cold pools. Cold-pool soundings coincide with (i) mesoscale cloud arcs and (ii) temperature drops of  $\sim 1$  K relative to the environment, along with moisture increases of  $\sim 1$  g kg<sup>-1</sup>. Furthermore, cold-pool moisture profiles exhibit a “moist layer” close to the surface, topped by a “dry layer” until the cloud base level, and followed by another moist layer in the cloud layer. In the presence of wind shear, the spreading of cold pools is favored downshear, suggesting downward momentum transport by unsaturated downdrafts. The results support the robustness of our detection method in diverse environmental conditions and its simplicity makes the method a promising tool for the characterization of cold pools, including their vertical structure. The applicability of the method to other regions and convective regimes is discussed.

**KEYWORDS:** Tropics; Cold pools; Soundings; Field experiments

## 1. Introduction

Below clouds, the partial evaporation of precipitation may cool the air sufficiently to generate unsaturated downdrafts, which spread horizontally when reaching the surface in the form of density currents. As these so-called cold pools expand, they lift the warmer adjacent air masses, leading in some situations to the creation of new convective cells (Craig Goff 1976; Warner et al. 1979; Böing et al. 2012; Torri et al. 2015; Li et al. 2014). This triggering has been observed to be particularly effective when two or more cold pools collide (Meyer and Haerter 2020; Droegemeier and Wilhelmson 1985; Feng et al. 2015; Torri and Kuang 2019; Haerter and Schlemmer 2018) or when the vorticity created by a cold pool counteracts that from the low-level wind shear (Rotunno et al. 1988; Weisman and Rotunno 2004; Bryan et al. 2006), although this latter result has been nuanced by subsequent studies (Lane and Moncrieff 2015; Tulich and Kiladis 2012; Grant et al. 2018). In addition, since they induce strong gusts near the surface, cold pools are suspected to enhance surface fluxes, and thus to modify the properties of the subcloud layer (SCL; Tompkins 2001; Langhans and Romps 2015; Schlemmer and Hohenegger 2016; Grant and van den Heever 2016; Gentine et al. 2016). For all these reasons, cold pools are thought to play an important role for the organization and the propagation of convection (Rotunno et al. 1988; Wakimoto 1982; Warner et al. 1980; Schlemmer and Hohenegger

2014; Tompkins 2001; Kurowski et al. 2018; Haerter and Schlemmer 2018; Muller and Bony 2015; Jeevanjee and Romps 2013).

Cold pools are ubiquitous in regions of precipitating convection, both over lands and oceans (Zipser 1977; Johnson and Nicholls 1983; Bryan and Parker 2010; Zuidema et al. 2017). Many past attempts to detect cold pools in observational data used methods based on surface time series. Analyzing data from the Tropical Ocean Global Atmosphere (TOGA) Coupled Ocean–Atmosphere Response Experiment (COARE; Webster and Lukas 1992), Young et al. (1995), for instance, defined the beginning of a cold-pool time period through the onset of rain rates of at least 2 mm h<sup>-1</sup> and the end of a cold-pool time period by the end of the subsequent surface temperature recovery. The choice of this threshold was motivated by a previous study of Barnes and Garstang (1982), which showed that only rainfall rates greater than 2 mm h<sup>-1</sup> were associated with penetrative rain-driven downdrafts. During the Rain in Cumulus over the Ocean campaign (RICO; Rauber et al. 2007), which took place in the eastern Caribbean from December 2004 to January 2005, Zuidema et al. (2012) used a similar method but did not impose any threshold on the surface rain rate, in order to consider all precipitating events. More recently, de Szoeke et al. (2017) detected cold pools over the central Indian Ocean during the Dynamics of the Madden–Julian Oscillation experiment (DYNAMO; Yoneyama et al. 2013) as temperature drops in the surface time series measured by the research vessel (R/V) *Roger Revelle*. A slightly modified version of this method was used in Vogel et al. (2021) to detect cold pools from 2011 to

Corresponding author: Nicolas Rochetin, nicolas.rochetin@lmd.ipsl.fr

2021 at the Barbados Cloud Observatory (BCO), a site exposed to relatively undisturbed trade winds on the eastern side of Barbados (Stevens et al. 2016).

Surface measurements from R/Vs or weather stations are useful to get data with high temporal resolution at a single point. They give precise information on the surface characteristics of cold pools, such as the wind shifts that they induce, the amplitude of the associated temperature drops, and their effects on surface fluxes. However, they say little about their vertical structure, in particular their height, which is recognized as an important parameter to describe the triggering of new convective cells near cold-pool edges (Grandpeix and Lafore 2010; Jeevanjee and Roms 2015). The distribution of temperature and moisture in and above cold pools is also poorly known (Zuidema et al. 2017), as is the distribution of horizontal and vertical winds.

The field study Elucidating the Role of Cloud–Circulation Coupling in Climate (EUREC<sup>4</sup>A; Bony et al. 2017; Stevens et al. 2021) might help overcome some of these difficulties. EUREC<sup>4</sup>A was held in January and February 2020 over the Atlantic Ocean east and south of Barbados and involved a wide variety of platforms: among others, four research aircraft, four R/Vs, surface observatories, and a battery of uncrewed aerial and seagoing systems. Aircraft and research vessels supported the implementation of a large-scale sounding array. In total, more than 2000 atmospheric profiles were measured during EUREC<sup>4</sup>A using radiosondes and dropsondes. This unprecedented dataset represents a unique opportunity to study the properties of cold pools over tropical oceans, provided that a robust method to detect cold pools from atmospheric soundings exists.

The lack of such a method motivates this study, which proposes a detection method of cold pools that is based on the height of the mixed layer and applies it to EUREC<sup>4</sup>A data. The paper is structured as follows: first, in section 2, we describe the EUREC<sup>4</sup>A radiosonde and dropsonde data used in this study. In section 3, we then present our detection method of cold pools and test it in a high-resolution simulation. We assess our detection method with EUREC<sup>4</sup>A data in section 4 and use it to provide a first analysis of cold pools during the field study.

## 2. Radiosonde and dropsonde data

During EUREC<sup>4</sup>A, atmospheric soundings were released in two different regimes: the “Trade Wind Alley” and the “Boulevard des Tourbillons” (Stevens et al. 2021). The Trade Wind Alley is a corridor up to 50°W east of Barbados, extending from approximately 11° to 17°N. In January and February, free-tropospheric subsidence prevails in these latitudes and the Trade Wind Alley can thus be seen as a trade wind regime, with shallow convective clouds under a capping inversion (Stevens et al. 2016). The Boulevard des Tourbillons is a corridor farther south extending from the northern coasts of Brazil to Barbados. It was initially chosen to characterize large-scale oceanic eddies observed along the coast of South America and their impact on air–sea interactions (Bony et al. 2017; Stevens et al. 2021). Located in areas of deeper

convection, the Boulevard des Tourbillons is also an opportunity to extend the EUREC<sup>4</sup>A sounding array down to the intertropical convergence zone.

In the Trade Wind Alley, both radiosondes and dropsondes were used to characterize the trade wind environment. Radiosondes were launched from land at BCO (13.16°N, 59.43°W) and from two R/Vs: the German R/V *Meteor*, cruising between 12° and 14.5°N at a fixed longitude of 57°W, and the American R/V from NOAA *Ronald H. Brown (RH-Brown)*, moving along transects farther to the east. The associated radiosonde datasets are described in Stephan et al. (2020). Two research aircraft, the German HALO and the WP-3D Orion (P-3) from NOAA, complemented this set of measurements by launching dropsondes. HALO flew at an altitude of about 10 km along the “EUREC<sup>4</sup>A circle,” a circular path with approximately 200-km diameter centered at 13.3°N, 57.7°W. When launching dropsondes, the P-3 flew at about 7 km along both linear and circular patterns mostly east of the EUREC<sup>4</sup>A circle around the nominal position of the *RH-Brown*, but also close to the Northwest Tropical Atlantic Station (NTAS) buoy near 51.02°W, 14.82°N, and around the EUREC<sup>4</sup>A circle. George et al. (2021) provide a detailed description of the dropsonde dataset. No dropsondes were launched in the Boulevard des Tourbillons, but radiosondes were launched from the French R/V *L’Atalante* and from the German R/V *Maria S. Merian (MS-Merian)*. Figure 1 shows a map of the measurement area with the ground position of the soundings launched by the different platforms.

Equipped with a GPS receiver, all of these radiosondes and dropsondes measured the pressure, temperature, humidity and horizontal wind along their fall or ascent. For radiosondes equipped with parachutes, we count the ascent and the descent as two separate profiles. In this study, we use quality controlled data (level 3) interpolated on a common altitude grid with bin sizes of 10 m (Stephan et al. 2020; George et al. 2021). In addition to the filters already used in the initial dataset, we are adding a filter to keep only soundings with at least 30 measurements of temperature, pressure, and humidity below 500 m. This filter is needed to get enough data in the lowest atmospheric layers to distinguish cold pools from their environment. It mainly affects descending profiles from radiosondes as their signal was sometimes lost in the first hundreds of meters above sea level due to Earth’s curvature (Stephan et al. 2020). It removes in total 441 radiosonde profiles, resulting in an input dataset with 1068 atmospheric profiles from dropsondes and 1105 from radiosondes. The sum of these radiosondes and dropsondes are referred to as the “EUREC<sup>4</sup>A soundings” throughout this study.

## 3. Presentation of the method and test in a high-resolution simulation

Most methods that have been proposed to detect cold pools from observations use the fact that the air inside a cold pool is colder than the air around it. The present detection method uses the fact that cold-pool air is colder than the air above it. As suggested by Rochetin et al. (2021), a spreading cold pool (in the form of a density current) enhances turbulence close

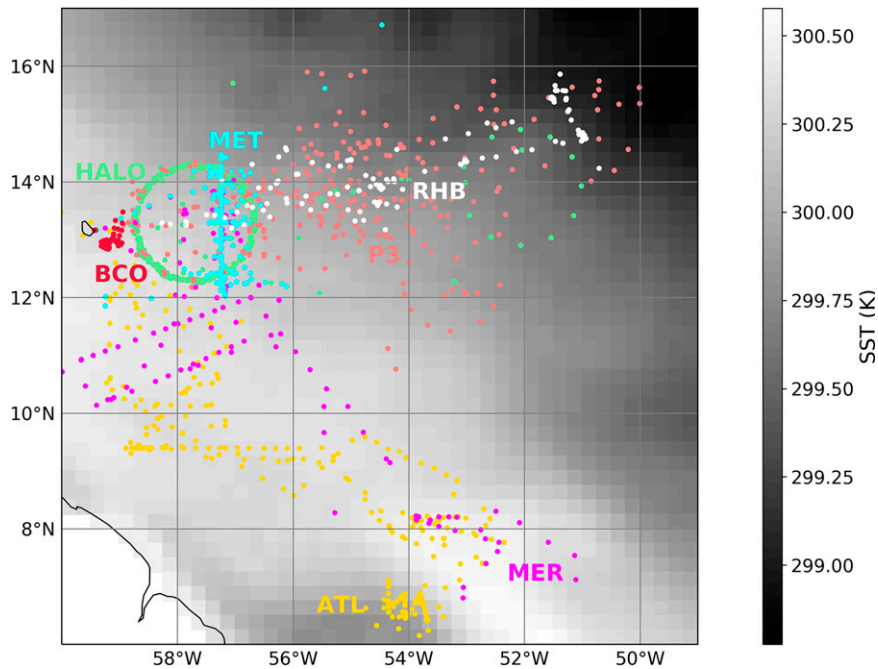


FIG. 1. The EUREC<sup>4</sup>A soundings used to detect cold pools: 1068 soundings from dropsondes and 1105 soundings from radiosondes. To build this dataset, we used level-3 soundings from George et al. (2021) and Stephan et al. (2020) with an additional filtering, described in the text. For radiosondes equipped with parachutes, we counted the ascent and the descent as two separate soundings. This resulted in a dataset composed of 810 dropsondes launched from HALO (HALO; light green), 258 from WP-3D (P3; salmon), as well as 249 radiosondes from BCO (BCO; red), 265 from Meteor (MET; cyan), 204 from RH-Brown (RHB; white), 265 from L'Atalante (ATL; gold), and 122 from MS-Merian (MER; magenta). Background shades show sea surface skin temperature (SST<sub>skin</sub>) from ERA5 reanalysis at 0.25° resolution averaged over January and February (Hennermann and Berrisford 2017). This figure is a modified version of Fig. 1 from Albright et al. (2021).

to the surface independent of the surface type and depth of convection. This enhanced turbulence generates a “mixed layer,” of depth  $H_{\text{mix}}$ , where the virtual potential temperature  $\theta_v$  is conserved. Over tropical oceans, the convective boundary layer is well-mixed in  $\theta_v$  across the whole SCL (Pennell and LeMone 1974; Cuijpers and Duynkerke 1993). Hence, a strong negative anomaly of  $H_{\text{mix}}$  is expected in oceanic cold pools, as shown in Rochetin et al. (2021), making  $H_{\text{mix}}$  a useful criterion to detect cold pools. On top of this mixed layer, a sharp increase in  $\theta_v$  is expected, referred to as the “stratified layer” in Rochetin et al. (2021). From Fig. 15 of Rochetin et al. (2021), one can roughly estimate the stratified-layer depth  $\sim 1\text{--}5$  times larger than the mixed-layer depth, depending on the convection development stage and the surface type. Following this line of thought, the cold-pool top  $H_{\text{top}}$  is then defined as the altitude where  $\theta_{v,\text{cold}} \simeq \theta_{v,\text{env}}$ . The SCL structure inside a cold pool can thus be summarized as a mixed layer topped by a stable stratified layer [see Fig. 1 of Rochetin et al. (2021) for an illustration of the conceptual picture underlying these physical considerations].

To identify cold pools in soundings based on  $H_{\text{mix}}$ , we follow Canut et al. (2012) and Rochetin et al. (2021) and define  $H_{\text{mix}}$  as the lowest altitude  $Z$  above  $Z_{\text{min}} = 100$  m where the

virtual potential temperature  $\theta_v$  is higher than its mass-weighted average from  $Z_{\text{min}}$  to  $Z$  by a fixed threshold  $\varepsilon = 0.2$  K:

$$\theta_v(Z) \geq \bar{\theta}_v + \varepsilon$$

$$\text{with } \bar{\theta}_v = \frac{\int_{Z_{\text{min}}}^Z \rho(z)\theta_v(z) dz}{\int_{Z_{\text{min}}}^Z \rho(z) dz}, \quad (1)$$

with  $\rho$  being the density of the air. Setting  $Z_{\text{min}}$  at 100 m is necessary due to the presence of unphysical temperature peaks below 100 m for a few radiosondes. The virtual potential temperature is calculated assuming that the air of the lowest layers is not saturated, so that the mixing ratio of liquid water in the air can be neglected. It is then approached as  $\theta_v = \theta(1 + 0.61r)$ ,  $r$  being the mixing ratio of water vapor. The calculation of  $H_{\text{mix}}$  thus requires only the vertical profiles of pressure, temperature and humidity at a single point and is directly applicable to soundings.

Figure 2 illustrates, through 3 instantaneous  $\theta_v$  profiles, the sensitivity of the  $H_{\text{mix}}$  estimate to  $\varepsilon$ . From Fig. 2 and visual inspection of several other profiles, the threshold of  $\varepsilon = 0.2$  K

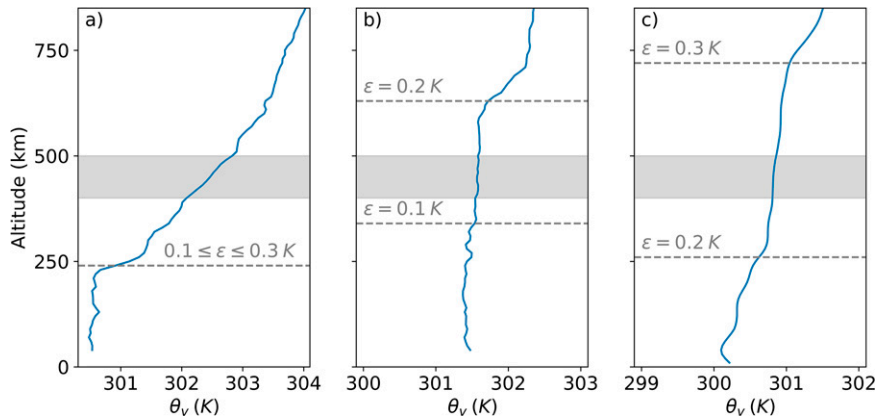


FIG. 2. (a)–(c) Profiles of virtual potential temperature between 0 and 800 m in three sounding profiles during EUREC<sup>4</sup>A, along with the mixed-layer height  $H_{\text{mix}}$  (dashed lines) for different values of the threshold  $\varepsilon$ . The shaded area between 400 and 500 m marks the separation between the cold-pool ( $H_{\text{mix}} \leq H_{\text{mix,cold}} = 400$  m) and environmental ( $H_{\text{mix}} \geq H_{\text{mix,env}} = 500$  m) soundings. In (a), whatever the choice of  $\varepsilon = 0.1, 0.2$ , or  $0.3$ , the profile is tagged as a cold-pool profile. In (b), the profile is tagged as a cold-pool profile if  $\varepsilon = 0.1$  and tagged as an environmental profile if  $\varepsilon = 0.2$  or  $0.3$ . In (c), the profile is tagged as a cold-pool profile if  $\varepsilon = 0.1$  or  $0.2$  and tagged as an environmental profile if  $\varepsilon = 0.3$ .

was found relevant to estimate a mixed-layer top. When the surface cooling is strong, Fig. 2a shows that any value of  $\varepsilon$  between 0.1 and 0.3 K gives the same value of  $H_{\text{mix}}$ . Nevertheless, Figs. 2b and 2c reveal that when vertical variations of  $\theta_v$  are weaker, a value of  $\varepsilon = 0.2$  K seems to better target the top of the mixed layer. Note that, as in Rochetin et al. (2021), we use  $\theta_v$  rather than  $\theta$  to calculate  $H_{\text{mix}}$  because we are mainly interested in cold pools that spread at the surface because of a difference of buoyancy relative to their environment, the latter depending both on temperature and specific humidity.

Figure 3 shows the  $H_{\text{mix}}$  distribution for EUREC<sup>4</sup>A soundings. The histogram reveals a negatively skewed distribution, with a median of  $\sim 720$  m. Besides cold pools, two phenomena can lead to stratification in the lowest layers of the atmosphere, and thus, to a decrease of  $H_{\text{mix}}$ : advection of warm air over a colder surface, and nocturnal surface radiative cooling (Mahrt 1998; Mason and Derbyshire 1990). The first situation arises typically when warm daytime air from land is advected over colder water (Smedman et al. 1993). As explained in Mahrt (1999) and Smedman et al. (1997), the stratification observed in this case is strongest near the coasts and attenuates progressively farther downstream as the air cools and the air–sea temperature difference reduces. Given the location of EUREC<sup>4</sup>A, downwind of the western Atlantic trade winds, warm air from lands would cool significantly before reaching the measurement area. Thus, it seems reasonable to reject this first hypothesis to explain the left tail of the  $H_{\text{mix}}$  distribution observed during EUREC<sup>4</sup>A.

The second potential source of stable boundary layers is net radiative cooling at night by the surface. Such radiative cooling is typically observed during clear nights over land. In such situations, the ground may lose a significant amount of heat by radiation and cool the adjacent air, leading to the

formation of a stably stratified inversion layer near the surface (Mahrt 1998; Grant 1997; Mahrt 2014). However, if net radiative cooling at night during EUREC<sup>4</sup>A was responsible for the left tail of the  $H_{\text{mix}}$  distribution, we would expect a diurnal

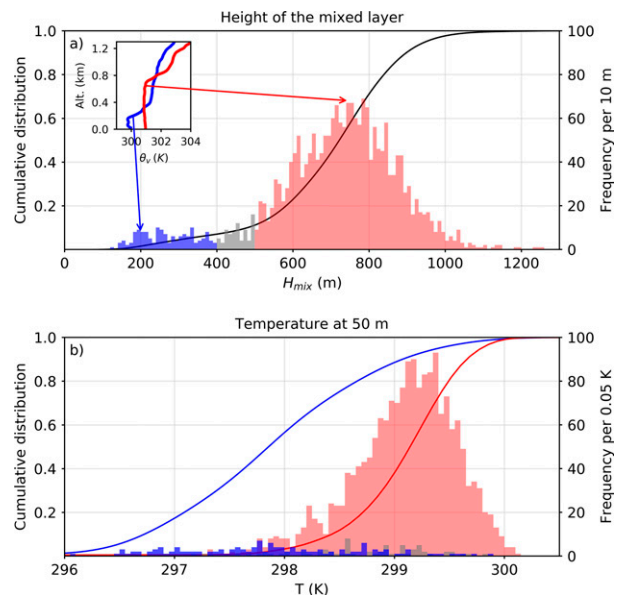


FIG. 3. (a) Cumulative distribution function (black) and histogram for the height of the mixed layer for all radiosondes and dropsondes launched during EUREC<sup>4</sup>A. The bins of the histogram are 10 m wide. Colors indicate cold-pool soundings (blue), unclassified soundings (gray), and environmental soundings (red). The inset shows two examples of  $\theta_v$  profiles, one in a cold pool and the other in the environment. (b) Cumulative distribution functions for cold-pool (blue), unclassified (gray), and environmental (red) temperatures at 50 m, and the corresponding histograms with a bin width of 0.05 K.

cycle of  $H_{\text{mix}}$ , contrary to what we find (not shown). The absence of a diurnal cycle in  $H_{\text{mix}}$  is expected from previous studies, which showed that the net radiative cooling near the surface is moderate at night during EUREC<sup>4</sup>A and more or less vertically homogeneous in the SCL (Albright et al. 2021, Fig. 3). Further, Vial et al. (2019) showed that the diurnal cycle of sea surface temperatures (SSTs) is weak in trade wind regimes. Given these observational results, we are confident that the nocturnal radiative cooling by the ocean surface is not strong enough to explain the left tail of the  $H_{\text{mix}}$  distribution on Fig. 3a.

Therefore, in the absence of other potential explanations, we attribute the left tail of  $H_{\text{mix}}$  distribution to cold pools. We choose to define “cold-pool soundings” as those with  $H_{\text{mix}}$  lower than a threshold  $H_{\text{mix,cold}} = 400$  m (7% of soundings, in blue), and “environmental soundings” as those with  $H_{\text{mix}}$  higher than  $H_{\text{mix,env}} = 500$  m (90% of soundings, in red). With this definition, only 3% of soundings (in gray) are neither in cold pools nor in the environment. The value of 500 m was chosen as a lower bound for the environmental soundings as it corresponds to the minimum SCL height observed during EUREC<sup>4</sup>A, on 26 January, under conditions of strong subsidence and low surface wind speed. The blue part of the  $H_{\text{mix}}$  distribution peaks slightly above 200 m. Hence, the corresponding cold-pool tops  $H_{\text{top}}$  might approach 400 m [taking into account of the stratified layer related in Rochetin et al. (2021)]. This is qualitatively consistent with Rochetin et al. (2021; Fig. 15d), where  $H_{\text{top}} \sim 400$  m is found for a cold pool simulated next to Barbados. Since this value is smaller by more than a factor of 2 than the typical mixed-layer height in the region (Fig. 3), the mixed-layer height seems to be a suitable criterion to distinguish cold pools from their environment during EUREC<sup>4</sup>A. In the boundary layer recovery process during the cold-pool dissipation (Grant and van den Heever 2016), the height of the mixed layer gradually increases due to surface sensible and latent heat fluxes and entrainment warming and drying from above, as documented by Zuidema et al. (2012) during RICO. It could explain the large spread of the  $H_{\text{mix}}$  distribution below 400 m (in blue) and its smooth increase from 400 to 500 m (in gray).

The surface temperature distribution (bottom panel, Fig. 3) reveals that cold-pool soundings are on average colder than environmental soundings. Nevertheless, given the spatial and temporal extent of EUREC<sup>4</sup>A, a fixed surface temperature threshold—as applied, for instance, in de Szoeko et al. (2017) to radiosondes launched from a single stationary R/V during DYNAMO—would not be able to isolate cold pools. Indeed, as illustrated in Fig. 1, cold pools are not the only source of variability for surface temperatures measured during EUREC<sup>4</sup>A, and there is, in particular, an SST difference of more than 1 K between the northeast (50°W, 16°N) and the southwest (59.5°W, 12°N) of the Trade Wind Alley. Pronounced mesoscale variability in SST features is also observed in the Boulevard des Tourbillons during the field study (Stevens et al. 2021). Because of this variability, the surface temperature distributions for cold-pool and environmental soundings overlap (as shown in Fig. 3b) and a fixed temperature threshold does not distinguish cold pools from their

environment over the large spatial scales considered within EUREC<sup>4</sup>A.

To show that the  $H_{\text{mix}}$  criterion robustly detects cold pools, we first test our detection method in a high-resolution simulation over the Atlantic Ocean, upstream of Barbados. This simulation was conducted using the large-eddy simulation (LES) version of the Icosahedral Nonhydrostatic (ICON) model, with 313-m horizontal grid spacing (Zängl et al. 2015; Dipankar et al. 2015). The LES vertical grid has 150 levels, with a resolution that progressively decreases with altitude: 20 m at the surface, about 70 m at 600-m height and about 80 m at 930-m height. The simulation uses the Smagorinsky turbulence scheme and the two-moment cloud microphysics parameterization of Seifert and Beheng (2006) but does not include any subgrid-scale cloud parameterization—the cloud fraction is 1 if the liquid water content is greater than  $10^{-5}$  kg kg<sup>-1</sup> (Vial et al. 2019; Vogel et al. 2021), and 0 otherwise. The LES is initialized on 11 December 2013 at 0900 UTC with 1.25 km-resolution runs and nudged at each time step to the 1.25-km simulation at its lateral boundaries. The 1.25-km simulation covers a larger domain and is itself initialized at 0000 UTC from Integrated Forecast System (IFS) data of the European Centre for Medium-Range Weather Forecasts (ECMWF) and nudged to the IFS data at its lateral boundaries every hour (Klocke et al. 2017).

In high-resolution models, most cold-pool detection methods rely on anomalies in surface temperature (or related quantities such as potential temperature or buoyancy), winds, or surface rain (see Drager and van den Heever 2017, and references therein). These methods usually require the full spatial fields of some thermodynamic or dynamic variables. Such spatial fields can easily be diagnosed from model outputs, but not from sounding data since the latter only provide 1D vertical profiles. Therefore, most detection methods used in high-resolution models cannot be directly applied to sounding data. On the contrary, our detection method is entirely local and can be applied in the same way to model outputs and sounding data, which is interesting if we want to compare the two. Such a comparison has been performed by Chandra et al. (2018) with time series from observations and model outputs but has never been conducted using a large dropsonde and radiosonde dataset such as that provided by EUREC<sup>4</sup>A.

Despite its simplicity, Fig. 4 shows that our detection method gives consistent results with the surface temperature and precipitation fields. This figure represents three snapshots of the mixed-layer height  $H_{\text{mix}}$  (left) and the temperature near the surface ( $z \approx 50$  m) (right) at 1600 UTC 11 December 2013 and at 0330 and 0930 UTC 12 December 2013. In the right panels, regions with negative temperature anomalies are collocated with significant surface precipitation (red dots) and also with important wind shifts (not shown), suggesting that these cold regions are in fact convective cold pools. In the left panels, we apply our detection method by circling in orange regions where  $H_{\text{mix}}$  is less than 400 m. Qualitatively, there is an excellent agreement between cold pools detected with our method and regions strongly cooled by rainfall.  $H_{\text{mix}}$  is unaffected by large-scale temperature gradients and seems to

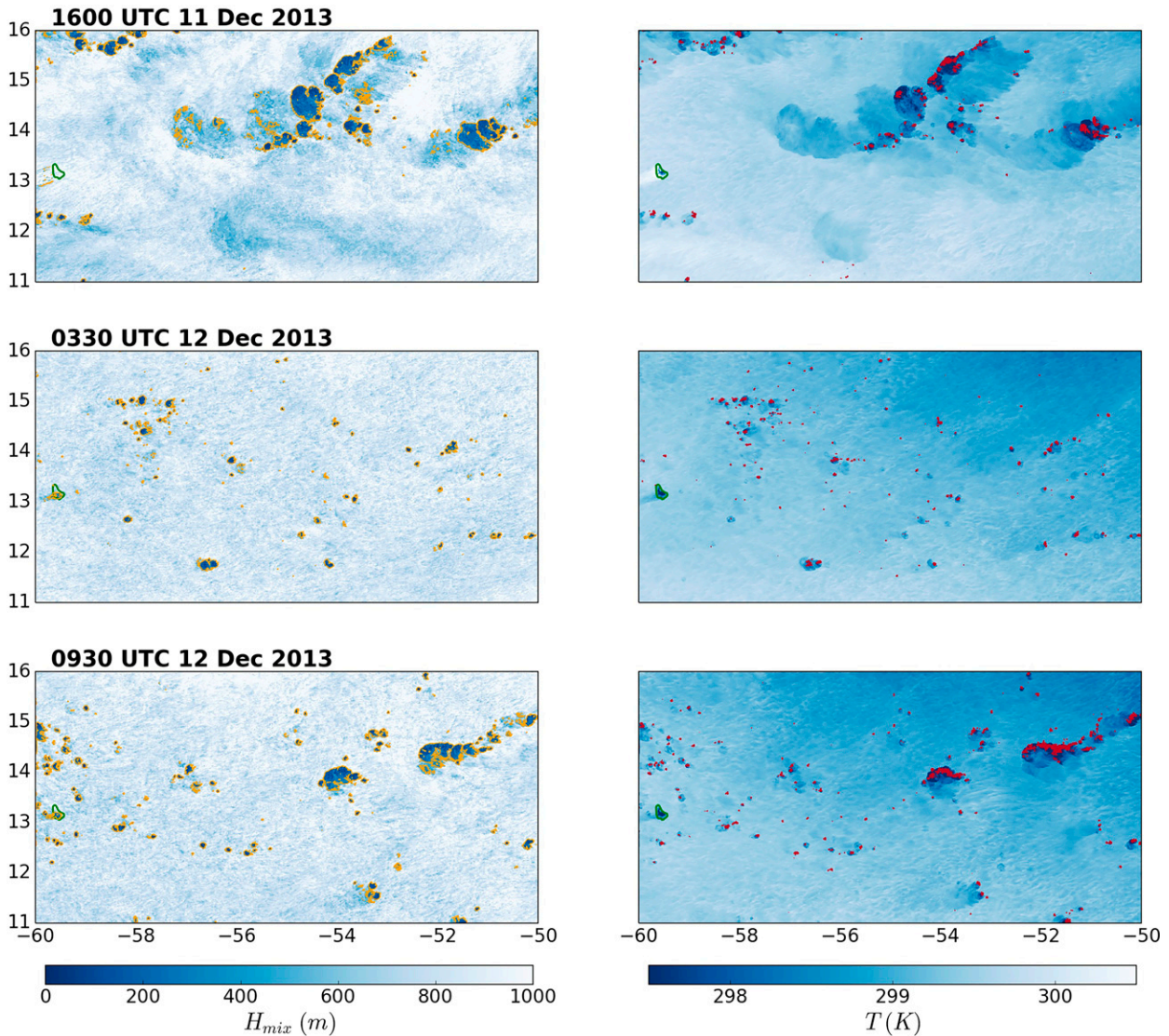


FIG. 4. The (left)  $H_{\text{mix}}$  and (right) surface temperature  $T$  at  $z \approx 50$  m simulated by ICON in an area of  $5^\circ \times 10^\circ$  upstream of Barbados (outlined in green) at 1600 UTC 11 Dec 2013 and at 0330 and 0930 UTC 12 Dec 2013. In the left panels, cold pools are circled in orange as regions where  $H_{\text{mix}}$  is lower than 400 m. In the right panels, the red dots represent locations where surface rainfall is greater than  $10 \text{ mm day}^{-1}$ .

discriminate cold pools almost everywhere in the domain. Conversely, precipitation alone is not a distinguishing factor of cold pools, as it is generally present only over a small part of the cold pools, and any method based on a temperature threshold would likely be strongly sensitive to the temperature gradient between the northeast and the southwest of the domain. This gives us confidence to choose  $H_{\text{mix}}$  in the next section to detect cold pools from soundings during EUREC<sup>4</sup>A. The choice of the threshold  $H_{\text{mix,cold}} = 400$  m might depend on (i) the surface conditions (land vs ocean), (ii) the convective regime (shallow vs deep), or (iii) the cold-pool life cycle stage (initial, mature, or decaying). The upper-left panel in Fig. 4 shows that the detection method does not capture the low  $H_{\text{mix}}$  pattern in the southern part of the

domain, and also misses parts of the mature cold pools near  $14^\circ\text{N}$ ,  $-56^\circ\text{E}$ . These features could be the imprint of a dissipating cold pool in which boundary layer recovery processes already acted to increase  $H_{\text{mix}}$  back to the pre-cold-pool value (Grant and van den Heever 2016). In summary, the use of  $H_{\text{mix}}$  enables a physically consistent detection of cold pools, while the choice of the threshold  $H_{\text{mix,cold}} = 400$  m—optimal for the EUREC<sup>4</sup>A soundings—has to be reconsidered and potentially adjusted when applied to other datasets.

To make some conjectures on the applicability of this simple method to other cases, one could first think about the potential case of cold pools higher than their environmental PBL (i.e., when  $H_{\text{top}} > H_{\text{pbl}}$ ). In such a case, the present method would not be affected in theory as long as  $H_{\text{mix}}$

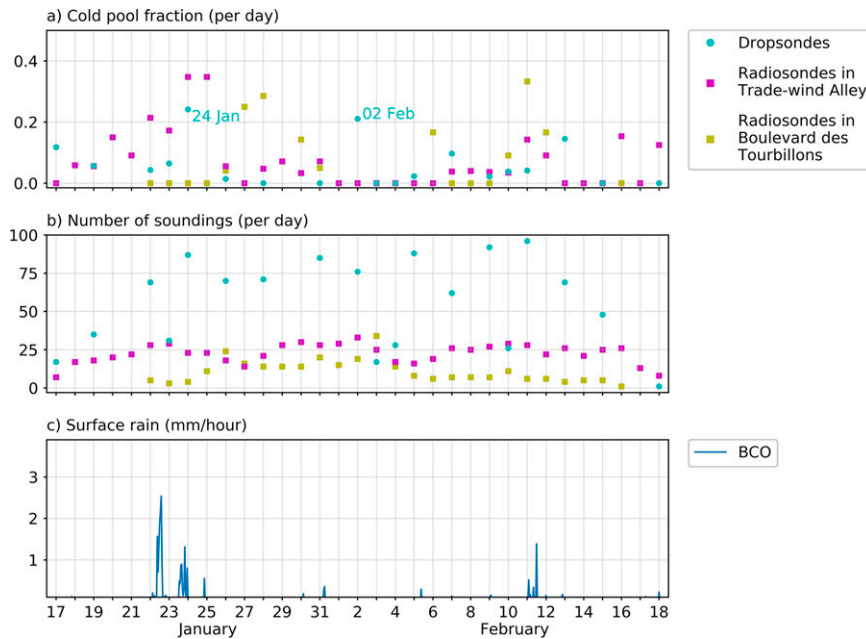


FIG. 5. (a) Cold-pool fraction per day from HALO and P-3 drospondes (cyan circles), and from radiosondes launched in the Trade Wind Alley (magenta squares) and in the Boulevard des Tourbillons (yellow squares). The two days selected for the case studies are indicated in cyan. (b) Number of soundings per day, with the same color code. (c) Hourly rain rate at BCO from the Micro Rain Radar at 325-m height [see Stevens et al. (2016) for details].

remains significantly lower than  $H_{\text{pbl}}$  inside cold pools [see Figs. 15b,c of Rochetin et al. (2021)]. However, in the case of a surface nocturnal inversion over a land surface strongly cooled overnight through radiation to space, in which the passage of a cold pool would induce a local positive  $H_{\text{mix}}$  anomaly [see Fig. 15a of Rochetin et al. (2021)], the present method might not work anymore. Indeed, the detection criterion would instead need to be “reversed,” such that  $H_{\text{mix}} > H_{\text{mix,cold}} \sim 0$ . Of course, none can say if these considerations—taken from a single numerical study—would hold in similar observed situations, but they might have to be kept in mind for future investigations, especially if one pursues the objective to generalize this simple detection method.

#### 4. Application to EUREC<sup>4</sup>A data

Applying our method to the set of 2174 EUREC<sup>4</sup>A soundings, we find that 149 “sondes” have fallen into cold pools. Figure 5 shows the cold-pool fraction (Fig. 5a), the number of soundings per day (Fig. 5b), and the hourly surface rain rate measured at BCO (Fig. 5c). As expected, we see some consistency between rain rates measured at BCO and cold-pool fraction in drospondes and radiosondes in the Trade Wind Alley—in particular, around 22–25 January and 11–12 February, when significant rainfall rates were measured at BCO. For the drospondes, the largest cold-pool fractions have been observed on 24 January and 2 February. In the

following, we will examine the cold-pool characteristics on these two days in more detail.

##### a. 24 January

On 24 January, more than 20% of drospondes (18 of 88; Fig. 5a) launched by HALO fell into cold pools. Figure 6a shows a MODIS *Terra* satellite image of that day, which reveals the presence of many mesoscale arcs. As noted by previous observational and modeling studies of trade wind regimes (Zuidema et al. 2012; Seifert and Heus 2013), such mesoscale arcs are likely due to cold pools. Indeed, while the dense air inside cold pools is less able to support buoyancy-driven convection, it has long been known that the edges of an expanding cold pool can lift surrounding air masses and trigger new convective cells (e.g., Purdom 1976; Knupp and Cotton 1982; Weisman and Rotunno 2004). Based on these previous studies, we expect relatively few clouds above cold pools, but mesoscale arcs of clouds near their border. The presence of many mesoscale arcs around the EUREC<sup>4</sup>A circle is thus consistent with the numerous cold pools detected that day from the HALO drospondes.

Superposing the launch positions of drospondes to GOES-16 visible channels reveals the cloud field that drospondes have actually sampled. Figure 6b (yellow box) shows the position of drospondes launched by HALO when passing over a mesoscale arc in the northeastern part of EUREC<sup>4</sup>A circle, just before 1400 UTC. Figures 6d and 6e give the potential

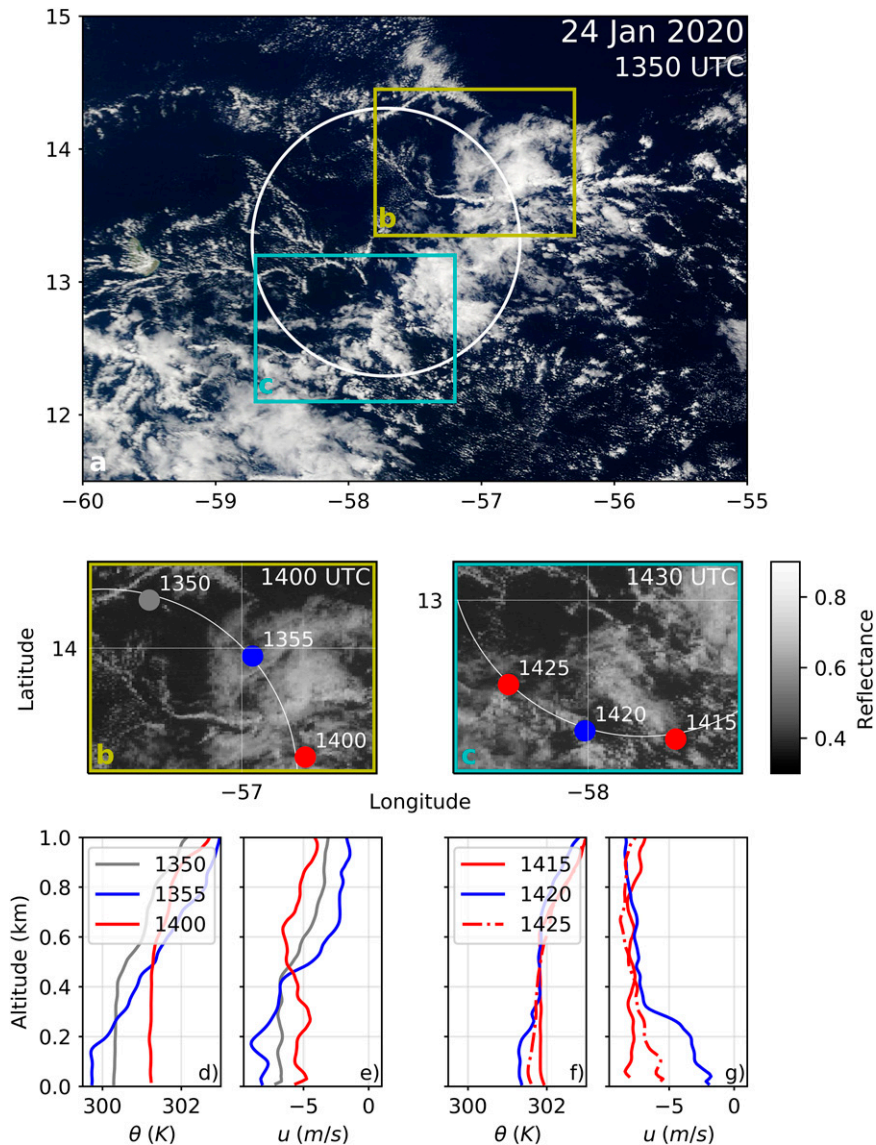


FIG. 6. (a) MODIS *Terra* scene from Worldview upstream of Barbados on 24 Jan 2020. The EUREC<sup>4</sup>A dropsonde circle is indicated in white. The rectangles mark the two regions shown in the lower panels. *GOES-16* visible reflectance (channel 2) is displayed at (b) 1400 UTC in the northeast quarter of the EUREC<sup>4</sup>A circle and at (c) 1430 UTC in the southwest part of the circle. The ground position and launch time of dropsondes dropped in the 15 min preceding the satellite image are shown in blue for cold-pool soundings, and in red for environmental soundings, and in gray for unclassified soundings. Also shown are profiles of (d),(f) potential temperature and (e),(g) zonal wind speed from the surface to 1 km for the dropsondes highlighted in (b) and (c).

temperature and zonal wind speed measured by these dropsondes. The cold-pool sounding (blue) is the coldest, with the strongest zonal wind near the surface and the shallowest mixed layer. In terms of potential temperature, mixed-layer height and zonal wind, the unclassified sounding (gray) represents an intermediate case between the cold-pool and the environmental (red) soundings. The unclassified sounding is located inside the mesoscale arc, but closer to its

edge than the cold-pool sounding, suggesting that the mixed layer may have partially recovered its initial properties near the cold pool.

Figure 6c (cyan box) gives a second example of a cold-pool sounding. Because of the presence of many clouds on the satellite image, it is hard to say whether the cold-pool sounding fell in a cloud arc. Our detection method seems nevertheless consistent with wind measurements, which

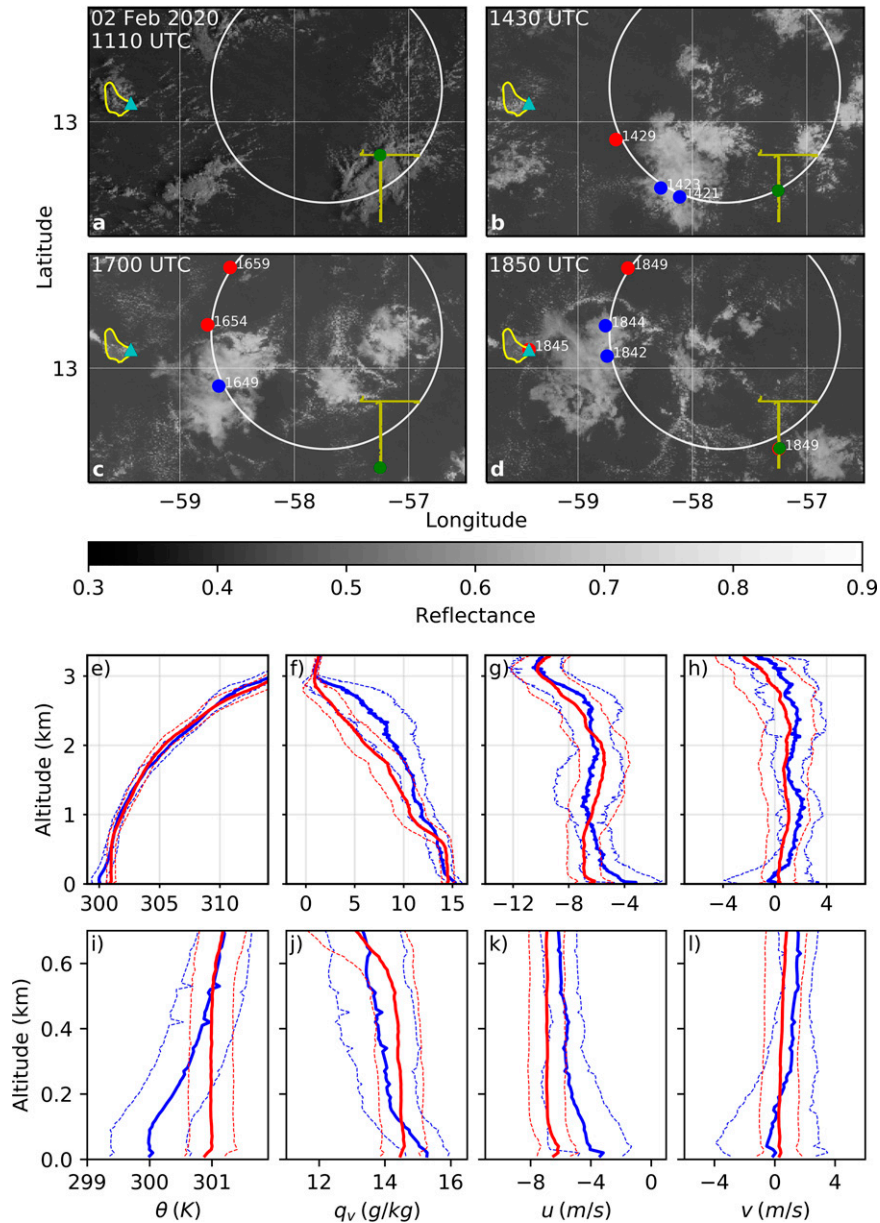


FIG. 7. *GOES-16* visible reflectance (channel 2), displayed at (a) 1130, (b) 1430, (c) 1700, and (d) 1850 UTC 2 Feb in the Atlantic region upstream Barbados (outlined in yellow). The EUREC<sup>4</sup>A circle is outlined in white. The ground position and launch time of dropsondes dropped in the 15 min preceding the satellite image are shown in blue for cold-pool soundings and in red for environmental ones. The yellow line represents the path of the *Meteor*, with the green-filled circle marking the position of the vessel at the time that the satellite image was taken. The location of BCO is indicated by a cyan triangle. (e) Mean potential temperature, (f) specific humidity, (g) zonal wind speed, and (h) meridional wind speed in cold-pool (blue) and environmental (red) soundings for that day. In each panel, the standard deviation around the mean for the two types of soundings is represented by a dashed line. (i)–(l) As in (e)–(h), with a focus on the SCL, between 0 and 700 m.

reveal the presence of a cold outflow at the surface (with a difference of more than  $3 \text{ m s}^{-1}$  in near-surface zonal velocity between the blue and red soundings). Note that in this example, clearly the surface temperature does not distinguish

cold pools, as the blue sounding (1419 UTC) in Fig. 6c is less than  $0.5 \text{ K}$  colder than the neighboring red soundings (1415 and 1424 UTC), and slightly warmer than the red sounding in Fig. 6b (1400 UTC).

*b. 2 February*

On 2 February, Figs. 7a–d show that the satellite images reveal a cloud field with many “flowers” [following the classification introduced in Stevens et al. (2019)], characterized by the presence of mesoscale, quasi-circular, stratiform shallow clouds, capped by a strong inversion and separated by very dry clear-sky areas. At 1700 and 1850 UTC, in the eastern part of the EUREC<sup>4</sup>A circle, a mesoscale cloud arc is visible in all directions around one of the flowers. As on 24 January, we suspect this cloud arc to be due to the presence of a cold pool at the surface. This suspicion is supported by the surface meteorological data from the research vessel *Meteor*, which captured a sudden drop of 1.5°C in surface temperature around 1110 UTC, marking the onset of the corresponding cold pool (see Fig. 8).

Sixteen of the 100 dropsondes and radiosondes launched near the EUREC<sup>4</sup>A circle that day were detected as cold pools; 13 of them fell in or around the cloud cluster passing over the *Meteor* at 1110 UTC. The three other cold-pool soundings all fell in the vicinity of other cloud clusters, located farther west of the EUREC<sup>4</sup>A circle (visible, e.g., at 1700 UTC in Fig. 7). In Fig. 7, mean sounding profiles in cold pools (blue) and in the environment (red) are shown in Figs. 7e–h and Figs. 7i–l.

From Figs. 7e and 7i, one can see that on 2 February cold pools are on average ~1 K colder than their surroundings in the firsts hundreds of meters, with an average mixed-layer  $H_{\text{mix}} \approx 100$  m. As from 500 m though, the  $\theta$  anomaly almost reduces to zero, meaning that the average height of cold pools  $H_{\text{top}} \approx 500$  m. For specific humidity  $q_v$ , things are more subtle: (i) close to the surface (i.e., in the first 100 m), a moist layer of 0.5–1 g kg<sup>-1</sup> is visible; (ii) across the remaining SCL (i.e., from 100 to 700 m), a dry layer of ~0.5 g kg<sup>-1</sup> is measured; (iii) and another moist layer is again observed in the cloud layer (i.e., from 700 to 3000 m). The opposite effects between surface evaporation due to surface fluxes strengthening in cold pools (Gentine et al. 2016) and dry air entrainment from unsaturated downdrafts under rain shafts (Grandpeix and Lafore 2010) might explain the complexity of  $q_v$  profile in the SCL. The subtle balance between these two effects might then have a great effects on the depths of the moist versus dry layers and on the amplitude of the moist and dry anomalies experienced in these layers. In addition to these internal effects, some external parameters like convection depth, background wind or SST might influence the cold-pool moisture profile. This result stresses the importance to investigate vertical profiles, in addition to 2D fields, for the study of cold pools.

The very subtle vertical distribution of specific humidity might also question the presence of the so-called moist rings, that is, regions of positive anomaly of specific humidity of ~1–2 g kg<sup>-1</sup> near the edges of cold pools, which have been reported in numerous numerical studies (Tompkins 2001; Seifert and Heus 2013; Li et al. 2014; Langhans and Romps 2015; Schlemmer and Hohenegger 2016; Torri et al. 2015; Feng et al. 2015). First, assuming that the strong  $q_v$  vertical gradients measured at low levels are ubiquitous in cold pools,

the estimate of  $q_{v,\text{low}}$  anomaly inside cold pools might be very sensitive to the altitude considered. As this statement holds for regions close to the cold-pool boundaries but still located inside cold pools, in which are frequently found the moist rings in numerical simulations, one can expect that the choice of the reference altitude for computing  $q_{v,\text{low}}$  might critically affect the moist rings occurrence and strength in these simulations. Second, numerical simulations might simply not capture well these strong  $q_v$  gradients at low levels. For these reasons, the quasi-systematic presence of moist rings at cold-pool boundaries in modeling studies is questionable and might deserve a meticulous revisitation. Indeed, a further exploration of the moisture profiles inside and around cold pools would then greatly help explaining the discrepancies between the modeling studies above mentioned and observational studies (e.g., Zuidema et al. 2012, 2017; de Szoeke et al. 2017; Vogel et al. 2021), which overall show very modest moist rings of ~0–0.3 g kg<sup>-1</sup> (although these observational studies show positive moisture anomalies when accounting for the whole cold-pool area, as this study will further show as well).

In the low levels, Figs. 7k and 7l show significant wind anomalies and variability inside cold pools. This is the “dynamical signature” of the cold-pool spreading motion, under the form of diverging density currents. Recent studies such as Garg et al. (2020, 2021) indeed use this wind signature (more specifically wind gradients) to detect deep convective cold pools from scatterometers onboard of orbiting satellites and generate a cold-pool climatology over tropical oceans. However, here again the mean vertical profile exposed in Figs. 7g and 7h shows that the wind anomaly inside cold pools changes of sign across the SCL, which is the mark of a strong wind shear in the low levels in cold pools. This aspect will be further explored in Figs. 9, 10, and 11.

Figure 8 shows time series of near-surface measurements collected on board of the R/V *Meteor* while crossing a cold pool on 2 February. From Fig. 8, time series show that the *Meteor* remained in the cold pool from 1100 UTC until 1230 UTC, when the temperature rose up to 26.2°C, a value slightly higher than before the passage of the cold pool. The wind speed (Fig. 8d) changed significantly as the ship passed through the cold-pool front: the absolute wind speed increased rapidly from 5 to 10 m s<sup>-1</sup> at the time of the temperature drop, before decreasing continuously to 2 m s<sup>-1</sup> and going back to its pre-cold-pool value of 5 m s<sup>-1</sup> after the cold pool passed. The wind speed variations upon entering and leaving the cold pool thus have approximately the same amplitude. These results stand both for the meridional and the zonal wind, although the wind shifts have slightly stronger amplitudes for the zonal wind. No general conclusion can be drawn from this single case; however, these results echo the study of Vogel et al. (2021) (where composite life cycle of cold pools have been derived from 11-yr BCO data) in the sense that the cold pool here sample similarly induces rapid variations in time series and that the horizontal moisture distribution across cold-pool

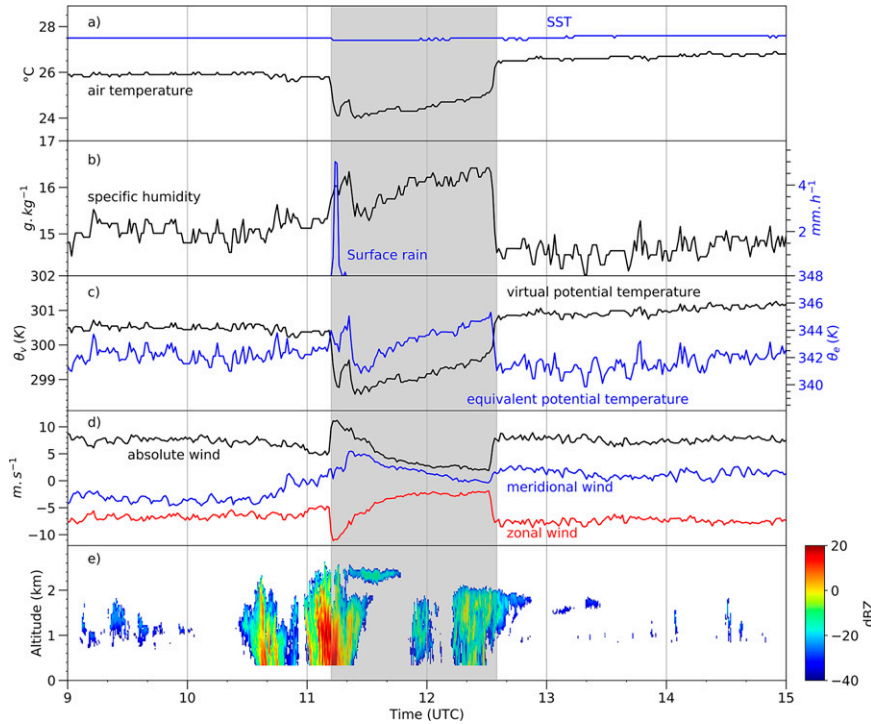


FIG. 8. Shipboard measurements from the *Meteor* from 0900 to 1500 UTC 2 Feb.: (a) surface air (black) and sea temperature (blue); (b) surface specific humidity (black) and surface rain rate (blue), measured using a ship rain gauge SRM 450; (c) virtual potential temperature (black) and equivalent potential temperature (blue); (d) zonal (red), meridional (blue) and absolute (black) wind speed; and (e) vertically pointing shipboard W-band radar data at 94 GHz, measured using the Raman lidar system Lidar for Cloud, Humidity and Temperature profiling (LICHT), formerly at BCO and described in Stevens et al. (2016). The color bar indicates uncalibrated radar signal-to-noise ratio, best interpreted relative to itself. In the five panels, the gray shading marks the cold-pool time period. *Meteor* data are freely accessible online (<https://observations.ipsl.fr/aeris/eurec4a/>).

transects is hard to interpret as it is very sensitive to the strength of cold pools (Vogel et al. 2021). As in Vogel et al. (2021) however, a modest moist ring of  $\sim 0.3 \text{ g kg}^{-1}$  is shown in Fig. 8. Ultimately, the horizontal and vertical

distribution of moisture in cold pools seems to respond to a subtle balance between effects of opposite signs, presumably driven by cold-pool internal dynamics and environmental factors.

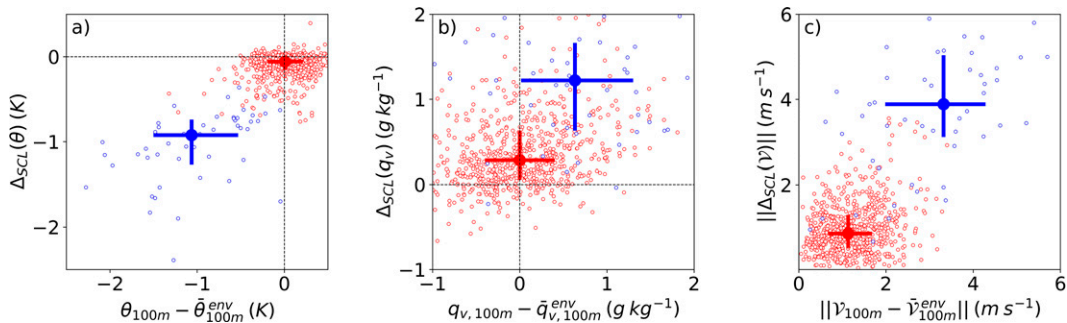


FIG. 9. Scatterplot of the vertical variations of (a) potential temperature  $\Delta_{SCL}(\theta)$ , (b) specific humidity  $\Delta_{SCL}(q_v)$ , and (c) wind speed  $\|\Delta_{SCL}(V)\|$  between 100 and 500 m vs spatial anomalies of the same variables at 100 m. The soundings considered are dropsondes launched in EUREC<sup>4</sup>A circles, and spatial anomalies are calculated with respect to the circle environmental mean, that is, the mean calculated circle by circle with dropsondes launched out of cold pools only. Also reported are the median values for cold pools (blue) and their environment (red). The bars indicate the 25th and 75th percentiles of the distributions.

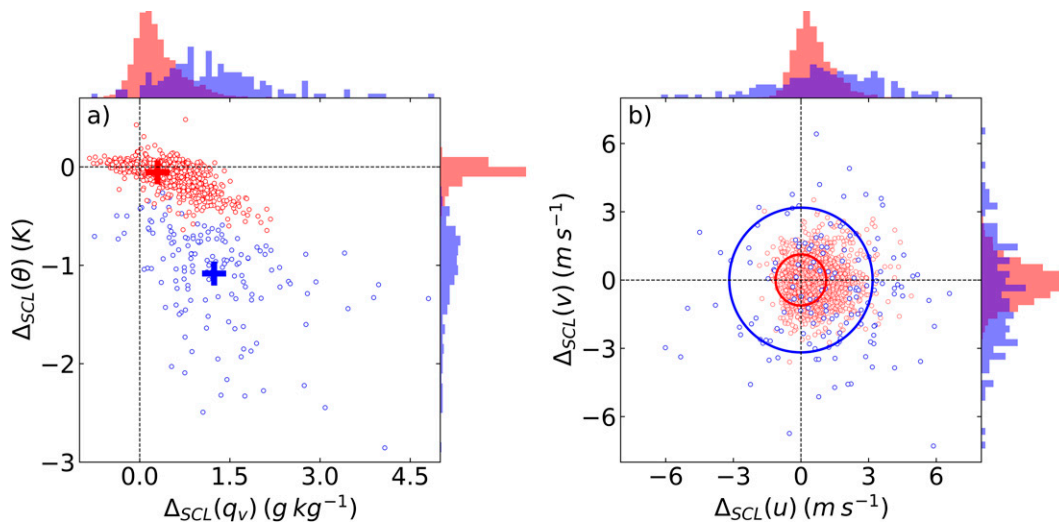


FIG. 10. (a) Scatterplot of the difference of potential temperature at 100 m and at 500 m  $\Delta_{SCL}(\theta)$  vs difference of specific humidity between the same altitudes  $\Delta_{SCL}(q_v)$  for cold-pool (blue) and environmental (red) soundings. The crosses indicate the mean of each distribution. On the top and right sides of the graph, marginal distributions of each variable are also reported for cold pools and their environment. The bins of the histograms are  $0.1 \text{ g kg}^{-1}$  wide for the specific humidity and  $0.1 \text{ K}$  wide for potential temperature. To facilitate the comparison, the area under each distribution has been normalized to 1. (b) As in (a), but for the meridional and zonal winds, with a bin width of  $0.3 \text{ m s}^{-1}$  for the corresponding histograms. The circles represent the mean of the absolute wind speed distributions, that is the mean of  $\sqrt{[\Delta_{SCL}(u)]^2 + [\Delta_{SCL}(v)]^2}$  for cold-pool and environmental soundings.

### c. Statistics for other days

We will now look at a few statistics of cold pools for other days during EUREC<sup>4</sup>A, focusing first on the HALO dropsondes launched in the EUREC<sup>4</sup>A circles. In total, the aircraft dropped more than 700 dropsondes along 72 circles, that is about 10 dropsondes per circle. We use circle sounding data to compare the characteristics of cold pools with those of their close environment. In Fig. 9, the  $x$  axis represents the difference between the potential temperature (Fig. 9a), specific humidity (Fig. 9b), and wind speed (Fig. 9c) measured by each dropsonde at 100 m and the mean value at the same altitude for environmental dropsondes launched in the same EUREC<sup>4</sup>A circle. Mathematically, we define in the following

$$X_{z_0} = 1/100 \text{ m} \int_{z_0-50 \text{ m}}^{z_0+50 \text{ m}} X(z) dz \text{ as the value of } X \text{ at the altitude}$$

$z_0$  averaged over a 100-m depth and  $\bar{X}_{z_0}^{\text{env}}$  as the mean circle value of  $X_{z_0}$  in environmental soundings. We average  $X_{z_0}$  over a 100-m interval so as to be less sensitive to local vertical heterogeneities. With these notations, the  $x$  axes become respectively  $\theta_{100\text{m}} - \bar{\theta}_{100\text{m}}^{\text{env}}$ ,  $q_{v,100\text{m}} - \bar{q}_{v,100\text{m}}^{\text{env}}$ , and  $\|V_{100\text{m}} - V_{100\text{m}}^{\text{env}}\|$ . These values of  $\theta$ ,  $q_v$ , and wind speed show that cold pools are on average  $1 \text{ K}$  colder and  $1 \text{ g kg}^{-1}$  moister than their environment and that the wind difference between individual soundings and mean circle values is on average  $2 \text{ m s}^{-1}$  larger for cold pools than for their environment. This positive moisture anomaly in EUREC<sup>4</sup>A cold pools is somehow consistent with the study of Vogel et al. (2021) who showed weaker humidity drops for weak cold pools, which are usually met in wintertime.

The  $y$  axis in Fig. 9 quantifies the imprint of cold pools on the vertical profiles for the same variables. For each sounding, the  $y$  coordinate represents the difference  $\Delta_{SCL}(X)$  in the SCL between 100 and 500 m, that is, in and above cold pools (when present). Mathematically, we define  $\Delta_{SCL}(X) = X_{100\text{m}} - X_{500\text{m}}$  for both cold-pool and environmental soundings. In the environment, on average, there is little difference in terms of potential temperature, specific humidity, and wind speed between the two layers, consistent with what we would expect for a relatively well-mixed layer. On the other hand, cold-pool soundings are on average  $1 \text{ K}$  cooler and  $1 \text{ g kg}^{-1}$  moister at 100 m, and the average wind difference is about  $3.5 \text{ m s}^{-1}$  between the two layers. These values are consistent with those of the  $x$  axis and suggest that in a well-mixed layer the vertical imprint of cold pools can be used to estimate the differences between cold pools and their environment in terms of potential temperature, specific humidity, and wind speed.

From these results, we take in Fig. 10 the vertical imprint of cold pools as a proxy to estimate the intensity of cold-pool anomalies. It allows us to generate statistics for all EUREC<sup>4</sup>A soundings, including the many radiosondes and dropsondes not launched in EUREC<sup>4</sup>A circles for which we do not have any environmental reference to assess cold-pool properties. Consistently with Fig. 9, cold-pool soundings are on average  $1 \text{ K}$  colder at 100 m than at 500 m, are  $1 \text{ g kg}^{-1}$  moister, and experience a wind difference between the two layers of  $2 \text{ m s}^{-1}$  larger than for environmental soundings. The coldest cold pools are also those for which the humidity difference is the most important, although potential temperature alone explains only a small part of the total humidity variance for

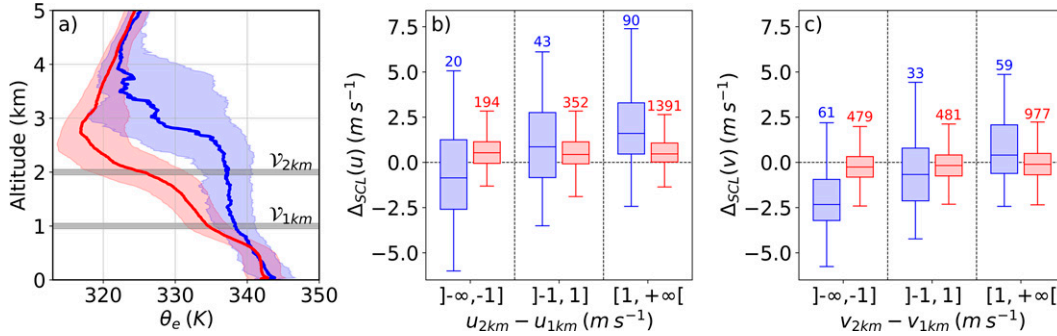


FIG. 11. (a) Profiles of equivalent potential temperature for all EUREC<sup>4</sup>A soundings launched in cold pools (blue) and in their environment (red). The thick lines represent the medians of each distribution, and the color shading is their interquartile range. The gray shading indicates the altitudes taken to define  $V_{1km} = (u_{1km}, v_{1km})$  and  $V_{2km} = (u_{2km}, v_{2km})$  used in (b) and (c). (b) Box-and-whisker plots for the zonal wind difference between 100 and 500 m [ $\Delta_{SCL}(u)$ ] for three ranges ( $x < -1$ ,  $-1 < x \leq 1$  and  $x > 1$ ) of zonal wind difference in the cloud layer computed as the difference between  $u_{2km} = \int_{1.8km}^{2.2km} u(z) dz$  and  $u_{1km} = \int_{0.8km}^{1.2km} u(z) dz$ , for each sounding. The horizontal line within each box represent the median, box bottom and top are first (Q1) and last (Q3) quartile of the distributions, and the whiskers extend up to  $1.5 \times$  interquartile range above Q3 and below Q1. The number of soundings used is indicated above each box-and-whisker plot. (c) As in (b), but for the meridional wind difference between 100 and 500 m  $\Delta_{SCL}(v)$  for three meridional wind shear ranges in the cloud layer.

cold-pool soundings ( $R^2 = 0.19$ ). The difference in humidity profiles in the SCL between cold pools and the environment is also visible in Fig. 11a, which gives the equivalent potential temperature in cold-pool and environmental soundings. Figure 11a further shows that cold-pool soundings are well mixed in equivalent potential temperature between 1 and 2.5 km, suggesting efficient moist convective mixing in the cloud layer above cold pools.

In Fig. 10b, the zonal and meridional wind distributions show that cold pools spread in all directions, consistently with the conceptual picture of a density current propagating over a solid boundary. In the presence of vertical wind shear, theories and numerical simulations nevertheless predict that cold-pool spreading may not be perfectly isotropic, as vertical momentum transport might favor the propagation of cold-pool downshear (Grant et al. 2020; Mahoney et al. 2009; Moncrieff 1992). Figure 11 middle and right panels test this hypothesis by showing the zonal and meridional wind difference between 100 and 500 m [ $\Delta_{SCL}(u)$  and  $\Delta_{SCL}(v)$ ] for three zonal and meridional wind difference ranges in the cloud layer, between 1 and 2 km:  $u_{2km} - u_{1km} \leq -1$ ,  $-1 < u_{2km} - u_{1km} \leq 1$  and  $u_{2km} - u_{1km} > 1$  (and the same for  $v_{2km} - v_{1km}$  in Fig. 11c). The box-and-whisker diagrams reveal that  $\Delta_{SCL}(u)$  is gradually shifted to higher values as the zonal wind shear in the cloud layer increases. On the contrary, in environmental soundings, the zonal wind shear in the cloud layer has little, if any, influence on  $\Delta_{SCL}(u)$ . The same result stands for the meridional wind, suggesting significant momentum transport by downdrafts in cold pools in all directions.  $\Delta_{SCL}(u)$  is higher than  $\Delta_{SCL}(v)$  for both cold-pool and environmental soundings because of strong zonal winds in this region, around  $-8.1 \text{ m s}^{-1}$  at 100 m on average, as compared with  $-1.7 \text{ m s}^{-1}$  at 100 m for mean meridional winds. These strong winds create

friction in the lowest layers and decrease  $u_{100m}$  with respect to  $u_{500m}$ , thus increasing  $\Delta_{SCL}(u)$ . These results provide a first systematic and robust characterization of cold pools over the wide range of conditions observed during EUREC<sup>4</sup>A, demonstrating how valuable detecting cold pools from soundings can be for the study of cold pools and cloud–circulation coupling.

## 5. Conclusions

In this study, we present a new method using the mixed-layer height  $H_{mix}$  as a criterion for detecting cold pools from soundings over tropical oceans. The method is applied to more than 2000 radiosondes and dropsondes from the EUREC<sup>4</sup>A field campaign that took place over the western tropical Atlantic near Barbados in January–February 2020. The mixed-layer height  $H_{mix}$ , defined using the virtual potential temperature, shows a left heavy tail for EUREC<sup>4</sup>A soundings that we attribute to cold pools. It leads us to classify the soundings with  $H_{mix} \leq H_{mix,cold} = 400 \text{ m}$  as cold-pool soundings, and those with  $H_{mix} \geq H_{mix,env} = 500 \text{ m}$  as environmental soundings.

We first test this criterion in a simulation upstream Barbados, performed with the LES version of the ICON model. In this simulation, cold pools are visually identified as regions with negative surface temperature anomalies and positive surface precipitation. They coincide with regions of shallow mixed layer, supporting the relevance of  $H_{mix}$  as a proxy to robustly identify cold pools in this simulation despite the presence of a strong SST gradient across the domain, since  $H_{mix}$  is here not affected by (i) large-scale SST patterns and (ii) diurnal variations of the solar forcing. The threshold of 400 m is optimal for the EUREC<sup>4</sup>A soundings and might have to be adapted for use with other datasets in other convection regimes, especially when dissipating mature cold pools should also be robustly identified.

We apply then our detection method to EUREC<sup>4</sup>A soundings, looking first at 24 January and 2 February, two EUREC<sup>4</sup>A flight days during which the number of cold pools detected in dropsondes is particularly high. On these two days, the cold pools detected with our method are consistent with satellite images, surface time series from the research vessel *Meteor*, and thermodynamic and dynamic profiles measured by soundings. The vertical profile of  $q_v$  anomaly inside cold pools exhibits (i) a moist layer close to the surface, (ii) a dry layer in the rest of the SCL, (iii) and a moist layer corresponding to the clouds topping cold pools. The complexity of the  $q_v$  profile might explain discrepancies between modeling and observational studies with regard to the hypothetical presence of moist rings surrounding cold pools, because it renders the estimate of  $q_v$  in the low levels very sensitive to the altitude considered, and numerical simulations might not correctly represent these steep  $q_v$  gradients.

We give a few statistics for the entire EUREC<sup>4</sup>A period, focusing initially on the dropsondes launched by HALO in the EUREC<sup>4</sup>A circle. By comparing, circle by circle, the cold pool and environmental characteristics, we find that at 100 m, the cold-pool soundings are on average 1 K colder and  $1 \text{ g kg}^{-1}$  moister than the environmental soundings at the same altitude and experience a wind deviation of more than  $3 \text{ m s}^{-1}$  with respect to their mean environment. We further show that these differences have a similar amplitude as the vertical differences between 100 and 500 m for each cold-pool sounding, while environmental soundings exhibit a small difference between these two altitudes, consistent with the well-mixed nature of the SCL in trade wind regimes. This significant vertical imprint of cold pools in the SCL is then studied for all the EUREC<sup>4</sup>A soundings. The coldest cold pools turn out to be those with the largest humidity difference between 100 and 500 m. When there is shear in the cloud layer, we find that the spreading of cold pools is favored downshear, suggesting momentum transport by unsaturated downdrafts feeding cold pools.

These first results and the method described here pave the way for more comprehensive analyses of cold pools over tropical oceans. The quantity and quality of the measurements made during EUREC<sup>4</sup>A is a great opportunity to perform such analyses. In particular, drones and low-flying aircraft are likely to provide valuable information on the vertical structure of cold pools, which could complement sounding measurements. In parallel, time series from research vessels and surface weather stations could help study the characteristics of cold pools close to the ground and better understand their interactions with the surface. The interest in cold pools in tropical oceans is not new (Zipser 1969; Leary and Houze 1979; Houze and Betts 1981), but EUREC<sup>4</sup>A offers an unprecedented dataset to finely characterize the temporal and spatial properties of cold pools and explore unanswered questions about their effect on the organization and propagation of convection. Hopefully, the method and results described in this paper will help us make the best use of this dataset and turn this opportunity into reality.

Ultimately, this study supports the statement that cold pools are ubiquitous over tropical oceans in shallow convection

regimes, in the presence of light precipitation. Moreover, although no formal evidence has been provided about their size and lifetime, one can suspect from satellite images that they might extend up to 100 km in diameter and last several hours, similarly to the deep convective cold pools. In the line of recent observational studies (Garg et al. 2020, 2021; Wills et al. 2021), which provided a cold-pool climatology at the tropical scale, the application of our detection method to a wider range of convective regimes and surface types is a clear objective to pursue (i) to better document tropical cold pools related to shallow and deep convection regimes and (ii) to investigate the potential similarities and differences between shallow and deep convective cold pools' internal dynamics.

*Acknowledgments.* Author Touzé-Peiffer gratefully acknowledges the funding of his Ph.D. by the AMX program of the Ecole Polytechnique. To access *GOES-16* visible data, this study benefited from the IPSL Prodiguer-Ciclad facility, which is supported by CNRS, UPMC, and Labex L-IPSL and funded by the ANR (Grant ANR-10-LABX-0018) and by the European FP7 IS-ENES2 project (Grant 312979). Author Vogel acknowledges funding from the European Research Council (ERC) under the European Union's Horizon 2020 Research and Innovation Programme (Grant Agreement 694768). The authors also thank the French Centre National d'Etudes Spatial (CNES) for funding this publication.

*Data availability statement.* The Python script used to compute the height of the mixed layer from sounding data is publicly released on Zenodo (<https://doi.org/10.5281/zenodo.5080277>, last accessed 20 July 2021; Touzé-Peiffer et al. 2021b). ICON primary data can be accessed through the "Mistral" super computer of the German Climate Computing Center/Deutsche Klimarechenzentrum (DKRZ). BCO Micro Rain Radar data are accessible to the broader community, as detailed in Stevens et al. (2016). Access to primary data is provided online (<https://mpimet.mpg.de/en/science/the-atmosphere-in-the-earth-system/working-groups/tropical-cloud-observation/barbadosstation1/instrumentation-and-data>). Radiosonde and dropsonde data are described respectively in Stephan et al. (2020) and George et al. (2021) and are available through the AERIS portal (<https://eurec4a.aeris-data.fr/>). Free access to *Meteor* surface meteorological data and Raman lidar data is also provided by AERIS. The MODIS *Terra* picture on January 24 is taken from NASA Worldview (<https://worldview.earthdata.nasa.gov>).

## APPENDIX A

### Satellite Movies

The snapshots shown in Figs. 6 and 7 provide an overview of the cloud fields in which soundings detected as cold pools have fallen during 24 January and 2 February, the two days where the largest cold-pool fractions have been measured by dropsondes. To facilitate the future use of our cold-pool dataset, we provide online a similar cold-pool

TABLE B1. Consistency between our sounding-based detection method and the time series-based detection method given in Vogel et al. (2021). For each radiosonde launched at BCO, on the *Meteor* or on the *RH-Brown*, we use the detection method of Vogel et al. (2021) to determine whether a cold pool is present in the surface temperature time series of the corresponding platform at the launch time of the radiosonde. The first column (agreement sounding/time series—in cold pools) indicates which fraction of the time steps flagged as cold pools at the launch time of a radiosonde in surface time series using Vogel et al. (2021) were also detected as cold pools in sounding data using our detection method. Reciprocally, the second column (agreement sounding/time series—in environment) indicates which fraction of the time steps flagged as environment at the launch time of a radiosonde were also detected as environment using our detection method. As detailed in the text, when the presence of a cold pool at the surface is ambiguous, e.g., because of missing data or near the beginning or the end of a cold pool, we flag the corresponding time steps as “unclassified.” The third column (number of unclassified soundings) gives the number of soundings whose launch time is unclassified in surface time series. The total number of soundings is given in the fourth column.

	Agreement soundings/time series		No. of unclassified soundings	Total no. of soundings
	In cold pools	In environment		
BCO	5/7 (71%)	160/169 (94%)	5	182
<i>Meteor</i>	4/4 (100%)	170/188 (90%)	27	219
<i>RH-Brown</i>	1/2 (50%)	85/89 (96%)	78	169
Total	10/13 (77%)	415/447 (93%)	110	570

tagging on satellite images for the whole campaign. To generate the corresponding movies, we used the 1 min mesoscans of the Advanced Baseline Imager (ABI) on board the *GOES-16* satellite ([GOES-R Calibration Working Group and GOES-R Series Program 2017](#)). The source code to generate the movies has already been used in Konow et al. (2021) and is freely available online (Fildier et al. 2021). For each EUREC<sup>4</sup>A day where ABI data are available, we generated two movies: the first using daytime reflectance (channel 2; 0.64  $\mu\text{m}$ ) from 1000 to 2200 UTC, and the second, using brightness temperature (channel 13; 10.35  $\mu\text{m}$ ) from 0000 to 2359 UTC. Channel 13 has a coarser resolution than channel 2 but has the advantage of being available day and night. We focused on the Trade Wind Alley, between 60° and 52°W and 10° and 16°N, where most radiosondes and dropsondes have fallen (as shown in Fig. 1). (The movies are available at <https://doi.org/10.25326/238>; Touzé-Peiffer et al. 2021a.)

## APPENDIX B

### Comparison with a Cold-Pool Detection Method from Time Series

We study here the consistency of our algorithm with the detection method used in Vogel et al. (2021) to detect cold pools from the BCO data. In this detection method, cold pools are identified as abrupt temperature drops in surface time series using the following procedure:

- 1) A smoothing is applied to the 1-min averaged time series with an 11-min running average and temperature drops  $\delta T = T_{\text{fil}}(t) - T_{\text{fil}}(t - 1) < -0.05$  K (per minute) in the filtered time series are identified as cold-pool candidates.
- 2) The onset of the cold-pool front  $t_{\text{max}}$  is then defined as the time of the last local temperature maximum  $T_{\text{max}}$  in the 20 min before the abrupt temperature drop. If the temperature is falling continuously within 20 min before the

temperature drop,  $t_{\text{max}}$  is taken as the time occurring 20 min before the abrupt temperature drop.

- 3) The end of the cold pool  $t_{\text{end}}$  is either defined (i) as the onset of the next cold pool, or (ii) as the time when the filtered temperature first exceeds its minimum by  $\Delta T/e$ , with  $\Delta T = T_{\text{max}} - T_{\text{min}}$ . If using condition (i) or (ii) leads to any temperature between  $t_{\text{min}}$  and  $t_{\text{end}}$  to be smaller than  $T_{\text{min}} - 0.1$  K, then  $t_{\text{end}}$  is defined as (iii) the time when the filtered temperature first decreases again after increasing for some time following  $t_{\text{min}}$ .

In Vogel et al. (2021), additional selection criteria are used to make the comparison of cold pools more robust. In particular, the authors consider only cold pools with  $\Delta T < -0.4$  K and less than two missing values in the filtered temperature time series during the entire cold-pool duration.

To evaluate the consistency of our detection method with surface time series, we apply the detection method used in Vogel et al. (2021) to the surface temperature time series measured at the BCO, on the R/V *Meteor*, and on the R/V *RH-Brown*. Each time step is flagged either as a “cold-pool time step,” as an “environmental time step,” or as an “unclassified time step.” All time steps with missing values in the temperature time series are flagged as unclassified. A quality flag is present in the *RH-Brown* dataset (as documented in Quinn et al. 2021) and we also consider as unclassified the data that do not meet the quality standards of this dataset. Moreover, we flag as unclassified the 11-min centered around the beginning and the end of each cold pool to account for the fact that Vogel et al. (2021) use a running average to detect cold pools, so their detection of the beginning and the end of cold pools is not as accurate. Similarly, the cold pools with more than two missing values in the filtered temperature time series as well as those that do not meet the threshold of  $\Delta T < -0.4$  K are flagged as unclassified. Once this unclassified time steps are defined, the algorithm of Vogel et al. (2021) is used to define cold-pool and environmental time steps in the surface time series.

For each ascending radiosonde launched at one of the three stations, we check whether the launch time of the radiosonde is detected as a cold-pool time step, an environmental time step, or an unclassified time step by the previous procedure and compare the result with that given by our detection method from sounding data. As shown in Table B1, the two methods qualitatively agree in most cases, both in cold pools and in their environment: 10 of the 13 time steps (77%) detected as cold pools in time series at the launch time of radiosondes were also detected as cold pools in sounding data and 415 of the 447 time steps (93%) detected as environment at the launch time of radiosondes were also detected as environment in sounding data. As the two methods are conceptually very different and use different datasets, these results seem encouraging and confirm the consistency between our detection method and the one used in Vogel et al. (2021) to detect cold pools.

## REFERENCES

- Albright, A. L., B. Fildier, L. Touzé-Peiffer, R. Pincus, J. Vial, and C. Muller, 2021: Atmospheric radiative profiles during EUREC<sup>4</sup>A. *Earth Syst. Sci. Data*, **13**, 617–630, <https://doi.org/10.5194/essd-13-617-2021>.
- Barnes, G. M., and M. Garstang, 1982: Subcloud layer energetics of precipitating convection. *Mon. Wea. Rev.*, **110**, 102–117, [https://doi.org/10.1175/1520-0493\(1982\)110<0102:SLEOPC>2.0.CO;2](https://doi.org/10.1175/1520-0493(1982)110<0102:SLEOPC>2.0.CO;2).
- Böing, S. J., H. J. Jonker, A. P. Siebesma, and W. W. Grabowski, 2012: Influence of the subcloud layer on the development of a deep convective ensemble. *J. Atmos. Sci.*, **69**, 2682–2698, <https://doi.org/10.1175/JAS-D-11-0317.1>.
- Bony, S., and Coauthors, 2017: EUREC<sup>4</sup>A: A field campaign to elucidate the couplings between clouds, convection and circulation. *Surv. Geophys.*, **38**, 1529–1568, <https://doi.org/10.1007/s10712-017-9428-0>.
- Bryan, G. H., and M. D. Parker, 2010: Observations of a squall line and its near environment using high-frequency rawinsonde launches during VORTEX2. *Mon. Wea. Rev.*, **138**, 4076–4097, <https://doi.org/10.1175/2010MWR3359.1>.
- , J. C. Knivel, and M. D. Parker, 2006: A multimodel assessment of RKW theory's relevance to squall-line characteristics. *Mon. Wea. Rev.*, **134**, 2772–2792, <https://doi.org/10.1175/MWR3226.1>.
- Canut, G., F. Couvreux, M. Lothon, D. Pino, and F. Saïd, 2012: Observations and large-eddy simulations of entrainment in the sheared Sahelian boundary layer. *Bound.-Layer Meteor.*, **142**, 79–101, <https://doi.org/10.1007/s10546-011-9661-x>.
- Chandra, A. S., P. Zuidema, S. Krueger, A. Kochanski, S. P. de Szoeké, and J. Zhang, 2018: Moisture distributions in tropical cold pools from equatorial Indian Ocean observations and cloud-resolving simulations. *J. Geophys. Res. Atmos.*, **123**, 11–445, <https://doi.org/10.1029/2018JD028634>.
- Craig Goff, R., 1976: Vertical structure of thunderstorm outflows. *Mon. Wea. Rev.*, **104**, 1429–1440, [https://doi.org/10.1175/1520-0493\(1976\)104<1429:VSOTO>2.0.CO;2](https://doi.org/10.1175/1520-0493(1976)104<1429:VSOTO>2.0.CO;2).
- Cuijpers, J., and P. Duynkerke, 1993: Large eddy simulation of trade wind cumulus clouds. *J. Atmos. Sci.*, **50**, 3894–3908, [https://doi.org/10.1175/1520-0469\(1993\)050<3894:LESOTW>2.0.CO;2](https://doi.org/10.1175/1520-0469(1993)050<3894:LESOTW>2.0.CO;2).
- de Szoeké, S. P., E. D. Skyllingstad, P. Zuidema, and A. S. Chandra, 2017: Cold pools and their influence on the tropical marine boundary layer. *J. Atmos. Sci.*, **74**, 1149–1168, <https://doi.org/10.1175/JAS-D-16-0264.1>.
- Dipankar, A., B. Stevens, R. Heinze, C. Moseley, G. Zängl, M. Giorgetta, and S. Brdar, 2015: Large eddy simulation using the general circulation model ICON. *J. Adv. Model. Earth Syst.*, **7**, 963–986, <https://doi.org/10.1002/2015MS000431>.
- Drager, A. J., and S. C. van den Heever, 2017: Characterizing convective cold pools. *J. Adv. Model. Earth Syst.*, **9**, 1091–1115, <https://doi.org/10.1002/2016MS000788>.
- Droegemeier, K. K., and R. B. Wilhelmson, 1985: Three-dimensional numerical modeling of convection produced by interacting thunderstorm outflows. Part II: Variations in vertical wind shear. *J. Atmos. Sci.*, **42**, 2404–2414, [https://doi.org/10.1175/1520-0469\(1985\)042<2404:TDNMOC>2.0.CO;2](https://doi.org/10.1175/1520-0469(1985)042<2404:TDNMOC>2.0.CO;2).
- Feng, Z., S. Hagos, A. K. Rowe, C. D. Burleyson, M. N. Martini, and S. P. de Szoeké, 2015: Mechanisms of convective cloud organization by cold pools over tropical warm ocean during the AMIE/DYNAMO field campaign. *J. Adv. Model. Earth Syst.*, **7**, 357–381, <https://doi.org/10.1002/2014MS000384>.
- Fildier, B., L. Touzé-Peiffer, and H. Schulz, 2021: bfieldier/EUREC4A\_movies: v1.0.0. Zenodo, <https://doi.org/10.5281/zenodo.4777954>.
- Garg, P., S. W. Nesbitt, T. J. Lang, G. Priftis, T. Chronis, J. D. Thayer, and D. A. Henc, 2020: Identifying and characterizing tropical oceanic mesoscale cold pools using spaceborne scatterometer winds. *J. Geophys. Res. Atmos.*, **125**, e2019JD031812, <https://doi.org/10.1029/2019JD031812>.
- , —, —, and —, 2021: Diurnal cycle of tropical oceanic mesoscale cold pools. *J. Climate*, **34**, 9305–9326, <https://doi.org/10.1175/JCLI-D-20-0909.1>.
- Gentine, P., A. Garelli, S.-B. Park, J. Nie, G. Torri, and Z. Kuang, 2016: Role of surface heat fluxes underneath cold pools. *Geophys. Res. Lett.*, **43**, 874–883, <https://doi.org/10.1002/2015GL067262>.
- George, G., and Coauthors, 2021: JOANNE: Joint Dropsonde Observations of the Atmosphere in Tropical North Atlantic Meso-Scale Environments. *Earth Syst. Sci. Data*, **13**, 5253–5272, <https://doi.org/10.5194/essd-13-5253-2021>.
- GOES-R Calibration Working Group and GOES-R Series Program, 2017: NOAA GOES-R series Advanced Baseline Imager (ABI) level 1b radiances. NOAA/National Centers for Environmental Information, accessed 20 January 2020, <https://doi.org/10.7289/V5BV7DSR>.
- Grandpeix, J.-Y., and J.-P. Lafore, 2010: A density current parameterization coupled with Emanuel's convection scheme. Part I: The models. *J. Atmos. Sci.*, **67**, 881–897, <https://doi.org/10.1175/2009JAS3044.1>.
- Grant, A. L. M., 1997: An observational study of the evening transition boundary-layer. *Quart. J. Roy. Meteor. Soc.*, **123**, 657–677, <https://doi.org/10.1002/qj.49712353907>.
- Grant, L. D., and S. C. van den Heever, 2016: Cold pool dissipation. *J. Geophys. Res. Atmos.*, **121**, 1138–1155, <https://doi.org/10.1002/2015JD023813>.
- , T. P. Lane, and S. C. van den Heever, 2018: The role of cold pools in tropical oceanic convective systems. *J. Atmos. Sci.*, **75**, 2615–2634, <https://doi.org/10.1175/JAS-D-17-0352.1>.
- , M. W. Moncrieff, T. P. Lane, and S. C. van den Heever, 2020: Shear-parallel tropical convective systems: Importance of cold pools and wind shear. *Geophys. Res. Lett.*, **47**, e2020GL087720, <https://doi.org/10.1029/2020GL087720>.

- Haerter, J. O., and L. Schlemmer, 2018: Intensified cold pool dynamics under stronger surface heating. *Geophys. Res. Lett.*, **45**, 6299–6310, <https://doi.org/10.1029/2017GL076874>.
- Hennemann, K., and P. Berrisford, 2017: ERA5 data documentation. Copernicus Climate Change Service, accessed 26 February 2020, <https://confluence.ecmwf.int/display/CKB/ERA5>.
- Houze, R. A., Jr., and A. K. Betts, 1981: Convection in GATE. *Rev. Geophys.*, **19**, 541–576, <https://doi.org/10.1029/RG019i004p00541>.
- Jeevanjee, N., and D. M. Romps, 2013: Convective self-aggregation, cold pools, and domain size. *Geophys. Res. Lett.*, **40**, 994–998, <https://doi.org/10.1002/grl.50204>.
- , and —, 2015: Effective buoyancy, inertial pressure, and the mechanical generation of boundary layer mass flux by cold pools. *J. Atmos. Sci.*, **72**, 3199–3213, <https://doi.org/10.1175/JAS-D-14-0349.1>.
- Johnson, R. H., and M. E. Nicholls, 1983: A composite analysis of the boundary layer accompanying a tropical squall line. *Mon. Wea. Rev.*, **111**, 308–319, [https://doi.org/10.1175/1520-0493\(1983\)111<0308:ACAOTB>2.0.CO;2](https://doi.org/10.1175/1520-0493(1983)111<0308:ACAOTB>2.0.CO;2).
- Klocke, D., M. Brueck, C. Hohenegger, and B. Stevens, 2017: Rediscovery of the doldrums in storm-resolving simulations over the tropical Atlantic. *Nat. Geosci.*, **10**, 891–896, <https://doi.org/10.1038/s41561-017-0005-4>.
- Knupp, K. R., and W. R. Cotton, 1982: An intense, quasi-steady thunderstorm over mountainous terrain. Part II: Doppler radar observations of the storm morphological structure. *J. Atmos. Sci.*, **39**, 343–358, [https://doi.org/10.1175/1520-0469\(1982\)039<0343:AIQSTO>2.0.CO;2](https://doi.org/10.1175/1520-0469(1982)039<0343:AIQSTO>2.0.CO;2).
- Konow, H., and Coauthors, 2021: EUREC4A's HALO. *Earth Syst. Sci. Data*, **13**, 5545–5563, <https://doi.org/10.5194/essd-13-5545-2021>.
- Kurowski, M. J., K. Suselj, W. W. Grabowski, and J. Teixeira, 2018: Shallow-to-deep transition of continental moist convection: Cold pools, surface fluxes, and mesoscale organization. *J. Atmos. Sci.*, **75**, 4071–4090, <https://doi.org/10.1175/JAS-D-18-0031.1>.
- Lane, T. P., and M. W. Moncrieff, 2015: Long-lived mesoscale systems in a low-convective inhibition environment. Part I: Upshear propagation. *J. Atmos. Sci.*, **72**, 4297–4318, <https://doi.org/10.1175/JAS-D-15-0073.1>.
- Langhans, W., and D. M. Romps, 2015: The origin of water vapor rings in tropical oceanic cold pools. *Geophys. Res. Lett.*, **42**, 7825–7834, <https://doi.org/10.1002/2015GL065623>.
- Leary, C. A., and R. A. Houze Jr., 1979: The structure and evolution of convection in a tropical cloud cluster. *J. Atmos. Sci.*, **36**, 437–457, [https://doi.org/10.1175/1520-0469\(1979\)036<0437:TSAEOC>2.0.CO;2](https://doi.org/10.1175/1520-0469(1979)036<0437:TSAEOC>2.0.CO;2).
- Li, Z., P. Zuidema, and P. Zhu, 2014: Simulated convective invigoration processes at trade wind cumulus cold pool boundaries. *J. Atmos. Sci.*, **71**, 2823–2841, <https://doi.org/10.1175/JAS-D-13-0184.1>.
- Mahoney, K. M., G. M. Lackmann, and M. D. Parker, 2009: The role of momentum transport in the motion of a quasi-idealized mesoscale convective system. *Mon. Wea. Rev.*, **137**, 3316–3338, <https://doi.org/10.1175/2009MWR2895.1>.
- Mahrt, L., 1998: Stratified atmospheric boundary layers and breakdown of models. *Theor. Comput. Fluid Dyn.*, **11**, 263–279, <https://doi.org/10.1007/s001620050093>.
- , 1999: Stratified atmospheric boundary layers. *Bound.-Layer Meteor.*, **90**, 375–396, <https://doi.org/10.1023/A:1001765727956>.
- , 2014: Stably stratified atmospheric boundary layers. *Annu. Rev. Fluid Mech.*, **46**, 23–45, <https://doi.org/10.1146/annurev-fluid-010313-141354>.
- Mason, P., and S. Derbyshire, 1990: Large-eddy simulation of the stably-stratified atmospheric boundary layer. *Bound.-Layer Meteor.*, **53**, 117–162, <https://doi.org/10.1007/BF00122467>.
- Meyer, B., and J. O. Haerter, 2020: Mechanical forcing of convection by cold pools: Collisions and energy scaling. *J. Adv. Model. Earth Syst.*, **12**, e2020MS002281, <https://doi.org/10.1029/2020MS002281>.
- Moncrieff, M. W., 1992: Organized convective systems: Archetypal dynamical models, mass and momentum flux theory, and parametrization. *Quart. J. Roy. Meteor. Soc.*, **118**, 819–850, <https://doi.org/10.1002/qj.49711850703>.
- Muller, C., and S. Bony, 2015: What favors convective aggregation and why? *Geophys. Res. Lett.*, **42**, 5626–5634, <https://doi.org/10.1002/2015GL064260>.
- Pennell, W., and M. LeMone, 1974: An experimental study of turbulence structure in the fair-weather trade wind boundary layer. *J. Atmos. Sci.*, **31**, 1308–1323, [https://doi.org/10.1175/1520-0469\(1974\)031<1308:AESOTS>2.0.CO;2](https://doi.org/10.1175/1520-0469(1974)031<1308:AESOTS>2.0.CO;2).
- Purdom, J. F., 1976: Some uses of high-resolution GOES imagery in the mesoscale forecasting of convection and its behavior. *Mon. Wea. Rev.*, **104**, 1474–1483, [https://doi.org/10.1175/1520-0493\(1976\)104<1474:SUOHRG>2.0.CO;2](https://doi.org/10.1175/1520-0493(1976)104<1474:SUOHRG>2.0.CO;2).
- Quinn, P. K., and Coauthors, 2021: Measurements from the RV *Ronald H. Brown* and related platforms as part of the Atlantic Tradewind Ocean-Atmosphere Mesoscale Interaction Campaign (ATOMIC). *Earth Syst. Sci. Data*, **13**, 1759–1790, <https://doi.org/10.5194/essd-13-1759-2021>.
- Rauber, R. M., and Coauthors, 2007: Rain in Shallow Cumulus over the Ocean: The RICO campaign. *Bull. Amer. Meteor. Soc.*, **88**, 1912–1928, <https://doi.org/10.1175/BAMS-88-12-1912>.
- Rochetin, N., C. Hohenegger, L. Touzé-Peiffer, and N. Villefranque, 2021: A physically-based definition of convectively generated density currents: Detection and characterization in convection-permitting simulations. *J. Adv. Model. Earth Syst.*, **13**, e2020MS002402, <https://doi.org/10.1029/2020MS002402>.
- Rotunno, R., J. B. Klemp, and M. L. Weisman, 1988: A theory for strong, long-lived squall lines. *J. Atmos. Sci.*, **45**, 463–485, [https://doi.org/10.1175/1520-0469\(1988\)045<0463:ATFSL>2.0.CO;2](https://doi.org/10.1175/1520-0469(1988)045<0463:ATFSL>2.0.CO;2).
- Schlemmer, L., and C. Hohenegger, 2014: The formation of wider and deeper clouds as a result of cold-pool dynamics. *J. Atmos. Sci.*, **71**, 2842–2858, <https://doi.org/10.1175/JAS-D-13-0170.1>.
- , and —, 2016: Modifications of the atmospheric moisture field as a result of cold-pool dynamics. *Quart. J. Roy. Meteor. Soc.*, **142**, 30–42, <https://doi.org/10.1002/qj.2625>.
- Seifert, A., and K. D. Beheng, 2006: A two-moment cloud microphysics parameterization for mixed-phase clouds. Part 1: Model description. *Meteor. Atmos. Phys.*, **92**, 45–66, <https://doi.org/10.1007/s00703-005-0112-4>.
- , and T. Heus, 2013: Large-eddy simulation of organized precipitating trade wind cumulus clouds. *Atmos. Chem. Phys.*, **13**, 5631–5645, <https://doi.org/10.5194/acp-13-5631-2013>.
- Smedman, A.-S., M. Tjernström, and U. Höglström, 1993: Analysis of the turbulence structure of a marine low-level jet. *Bound.-Layer Meteor.*, **66**, 105–126, <https://doi.org/10.1007/BF00705462>.
- , H. Bergström, and B. Grisogono, 1997: Evolution of stable internal boundary layers over a cold sea. *J. Geophys. Res.*, **102**, 1091–1099, <https://doi.org/10.1029/96JC02782>.
- Stephan, C. C., and Coauthors, 2020: Ship-and island-based atmospheric soundings from the 2020 EUREC<sup>4</sup>A field campaign.

- Earth Syst. Sci. Data*, **13**, 491–514, <https://doi.org/10.5194/essd-2020-174>.
- Stevens, B., and Coauthors, 2016: The Barbados Cloud Observatory: Anchoring investigations of clouds and circulation on the edge of the ITCZ. *Bull. Amer. Meteor. Soc.*, **97**, 787–801, <https://doi.org/10.1175/BAMS-D-14-00247.1>.
- , and Coauthors, 2019: Sugar, gravel, fish and flowers: Mesoscale cloud patterns in the trade winds. *Quart. J. Roy. Meteor. Soc.*, **146**, 141–152, <https://doi.org/10.1002/qj.3662>.
- , and Coauthors, 2021: EUREC<sup>4</sup>A. *Earth Syst. Sci. Data*, **13**, 4067–4119, <https://doi.org/10.5194/essd-13-4067-2021>.
- Tompkins, A. M., 2001: Organization of tropical convection in low vertical wind shears: The role of cold pools. *J. Atmos. Sci.*, **58**, 1650–1672, [https://doi.org/10.1175/1520-0469\(2001\)058<1650:OOTCIL>2.0.CO;2](https://doi.org/10.1175/1520-0469(2001)058<1650:OOTCIL>2.0.CO;2).
- Torri, G., and Z. Kuang, 2019: On cold pool collisions in tropical boundary layers. *Geophys. Res. Lett.*, **46**, 399–407, <https://doi.org/10.1029/2018GL080501>.
- , —, and Y. Tian, 2015: Mechanisms for convection triggering by cold pools. *Geophys. Res. Lett.*, **42**, 1943–1950, <https://doi.org/10.1002/2015GL063227>.
- Touzé-Peiffer, L., R. Vogel, and N. Rochetin, 2021a: GOES-16 ABI movies (VIS+IR) with cold pool tagging. AERIS, <https://doi.org/10.25326/238>.
- , —, and —, 2021b: ludotzp/JAMC-HMIX-2021: First release of Hmix computation. Zenodo, accessed 20 July 2021, <https://doi.org/10.5281/zenodo.5080278>.
- Tulich, S. N., and G. N. Kiladis, 2012: Squall lines and convectively coupled gravity waves in the tropics: Why do most cloud systems propagate westward? *J. Atmos. Sci.*, **69**, 2995–3012, <https://doi.org/10.1175/JAS-D-11-0297.1>.
- Vial, J., and Coauthors, 2019: A new look at the daily cycle of trade wind cumuli. *J. Adv. Model. Earth Syst.*, **11**, 3148–3166, <https://doi.org/10.1029/2019MS001746>.
- Vogel, R., H. Konow, H. Schulz, and P. Zuidema, 2021: A climatology of trade-wind cumulus cold pools and their link to mesoscale cloud organization. *Atmos. Chem. Phys.*, **21**, 16 609–16 630, <https://doi.org/10.5194/acp-21-16609-2021>.
- Wakimoto, R. M., 1982: The life cycle of thunderstorm gust fronts as viewed with Doppler radar and rawinsonde data. *Mon. Wea. Rev.*, **110**, 1060–1082, [https://doi.org/10.1175/1520-0493\(1982\)110<1060:TLCOTG>2.0.CO;2](https://doi.org/10.1175/1520-0493(1982)110<1060:TLCOTG>2.0.CO;2).
- Warner, C., J. Simpson, D. Martin, D. Suchman, F. Mosher, and R. Reinking, 1979: Shallow convection on day 261 of GATE/mesoscale arcs. *Mon. Wea. Rev.*, **107**, 1617–1635, [https://doi.org/10.1175/1520-0493\(1979\)107<1617:SCODOG>2.0.CO;2](https://doi.org/10.1175/1520-0493(1979)107<1617:SCODOG>2.0.CO;2).
- , —, G. V. Helvoirt, D. Martin, D. Suchman, and G. Austin, 1980: Deep convection on day 261 of GATE. *Mon. Wea. Rev.*, **108**, 169–194, [https://doi.org/10.1175/1520-0493\(1980\)108<0169:DCODOG>2.0.CO;2](https://doi.org/10.1175/1520-0493(1980)108<0169:DCODOG>2.0.CO;2).
- Webster, P. J., and R. Lukas, 1992: TOGA COARE: The Coupled Ocean–Atmosphere Response Experiment. *Bull. Amer. Meteor. Soc.*, **73**, 1377–1416, [https://doi.org/10.1175/1520-0477\(1992\)073<1377:TCTCOR>2.0.CO;2](https://doi.org/10.1175/1520-0477(1992)073<1377:TCTCOR>2.0.CO;2).
- Weisman, M. L., and R. Rotunno, 2004: “A theory for strong long-lived squall lines” revisited. *J. Atmos. Sci.*, **61**, 361–382, [https://doi.org/10.1175/1520-0469\(2004\)061<0361:ATFSL>2.0.CO;2](https://doi.org/10.1175/1520-0469(2004)061<0361:ATFSL>2.0.CO;2).
- Wills, S. M., M. F. Cronin, and D. Zhang, 2021: Cold pools observed by uncrewed surface vehicles in the central and eastern tropical Pacific. *Geophys. Res. Lett.*, **48**, e2021GL093373, <https://doi.org/10.1029/2021GL093373>.
- Yoneyama, K., C. Zhang, and C. N. Long, 2013: Tracking pulses of the Madden–Julian oscillation. *Bull. Amer. Meteor. Soc.*, **94**, 1871–1891, <https://doi.org/10.1175/BAMS-D-12-00157.1>.
- Young, G. S., S. M. Perugini, and C. W. Fairall, 1995: Convective wakes in the equatorial western Pacific during TOGA. *Mon. Wea. Rev.*, **123**, 110–123, [https://doi.org/10.1175/1520-0493\(1995\)123<0110:CWITEW>2.0.CO;2](https://doi.org/10.1175/1520-0493(1995)123<0110:CWITEW>2.0.CO;2).
- Zängl, G., D. Reinert, P. Rípodas, and M. Baldauf, 2015: The ICON (ICOsahedral Non-hydrostatic) modelling framework of DWD and MPI-M: Description of the non-hydrostatic dynamical core. *Quart. J. Roy. Meteor. Soc.*, **141**, 563–579, <https://doi.org/10.1002/qj.2378>.
- Zipser, E. J., 1969: The role of organized unsaturated convective downdrafts in the structure and rapid decay of an equatorial disturbance. *J. Appl. Meteor.*, **8**, 799–814, [https://doi.org/10.1175/1520-0450\(1969\)008<0799:TROUC>2.0.CO;2](https://doi.org/10.1175/1520-0450(1969)008<0799:TROUC>2.0.CO;2).
- , 1977: Mesoscale and convective-scale downdrafts as distinct components of squall-line structure. *Mon. Wea. Rev.*, **105**, 1568–1589, [https://doi.org/10.1175/1520-0493\(1977\)105<1568:MACDAD>2.0.CO;2](https://doi.org/10.1175/1520-0493(1977)105<1568:MACDAD>2.0.CO;2).
- Zuidema, P., and Coauthors, 2012: On trade wind cumulus cold pools. *J. Atmos. Sci.*, **69**, 258–280, <https://doi.org/10.1175/JAS-D-11-0143.1>.
- , G. Torri, C. Muller, and A. Chandra, 2017: A survey of precipitation-induced atmospheric cold pools over oceans and their interactions with the larger-scale environment. *Surv. Geophys.*, **38**, 1283–1305, <https://doi.org/10.1007/s10712-017-9447-x>.